*Pro‐L * ‐ A probabilistic L * mapping tool for ground observations*

Space Weather

RESEARCH ARTICLE
10.1029/2020SW002602

Pro-*L** - A Probabilistic *L** Mapping Tool for Ground Observations

Rhys L. Thompson[1], Steven K. Morley[2], Clare E. J. Watt[3], Sarah N. Bentley[3], and Paul D. Williams[3]

[1]Department of Mathematics and Statistics, University of Reading, Reading, UK, [2]Space Science and Applications, Los Alamos National Laboratory, Los Alamos, NM, USA, [3]Department of Meteorology, University of Reading, Reading, UK

Key points:

- Pro-*L** uses multiple magnetic field models to estimate *L** corresponding to ground footprints across the Northern Hemisphere
- The use of multiple models reduces systematic bias from single models, and introduces variability which informs us of model weaknesses
- Pro-*L** is a rapid alternative to computationally expensive standard techniques and quantifies inherent uncertainty from model biases

Supporting Information:

- Supporting Information S1
- Data Set S1
- Data Set S2
- Data Set S3
- Data Set S4
- Data Set S5
- Data Set S6
- Data Set S7
- Data Set S8
- Data Set S9
- Data Set S10
- Data Set S11
- Data Set S12
- Data Set S13
- Data Set S14
- Figure S1
- Figure S2
- Figure S3
- Figure S4
- Figure S5

Correspondence to:

R. L. Thompson,
r.l.thompson@pgr.reading.ac.uk

Citation:

Thompson, R. L., Morley, S. K., Watt, C. E. J., Bentley, S. N., & Williams, P. D. (2021). Pro-*L** - A probabilistic *L** mapping tool for ground observations. *Space Weather*, *18*, e2020SW002602. https://doi.org/10.1029/2020SW002602

Received 4 AUG 2020
Accepted 11 DEC 2020

Abstract Both ground and space observations are used extensively in the modeling of space weather processes within the Earth's magnetosphere. In radiation belt physics modeling, one of the key phase-space coordinates is *L**, which indicates the location of the drift paths of energetic electrons. Global magnetic field models allow a subset of locations on the ground (mainly subauroral) to be mapped along field lines to a location in space and transformed into *L**, provided that the initial ground location maps to a closed drift path. This allows observations from ground, or low-altitude space-based platforms to be mapped into space in order to inform radiation belt modeling. Many data-based magnetic field models exist; however, these models can significantly disagree on mapped *L** values for a single point on the ground, during both quiet times and storms. We present a state of the art probabilistic *L** mapping tool, Pro-*L**, which produces probability distributions for *L** corresponding to a given ground location. Pro-*L** has been calculated for a high resolution magnetic latitude by magnetic local time grid in the Earth's Northern Hemisphere. We have developed the probabilistic model using 11 years of *L** calculations for seven widely used magnetic field models. Usage of the tool is highlighted for both event studies and statistical models, and we demonstrate a number of potential applications.

Plain Language Summary Observations made by ground and space based instruments are used extensively in modeling of space weather processes within the Earth's radiation belts, regions of charged and energetic particles trapped by Earth's magnetic field. The shape of the magnetic field is not fixed, however, and there is not a consistent relationship between the footprint location of a ground measurement and its respective position in space. With no way to validate the global true magnetic field, numerous models exist to approximate it. We often envision the radiation belts in a fixed coordinate system representative of the motions of the trapped particles. Often considered a proxy for distance is *L**, a quantity related to the radial motion of electrons. Once an observation's respective location in the magnetic field is approximated it can be transformed into *L**, provided the electrons at the measurement's physical location remain trapped. Dependency of *L** on magnetic field model accuracy is paramount, yet models can significantly disagree on the *L** of colocated observations. We present a state-of-the-art tool, Pro-*L**, which for any ground observation provides the probabilities of corresponding *L** values. Usage is highlighted for both event studies and statistical models, and we demonstrate a number of potential applications.

1. Introduction

The operational and research-focused modeling of high-energy electron fluxes in Earth's radiation belts is based upon the physics of electron motion in the Earth's magnetic field. High-energy electrons are trapped in the approximately dipolar magnetic field and execute three motions: very fast gyromotion (with periods of less than 1 ms), fast bounce motion between hemispheres (with periods of ~1 s) and drift motion around the planet (with periods of minutes). Models of radiation belt dynamics use a coordinate system based upon these motions, which can be described using a system of adiabatic invariants μ, J, and L^*. This means that slow, reversible changes to the energy and path of electrons due to slow changes in the magnetic field are automatically taken into account in the model, since the computational grids themselves are based upon the invariant. It therefore becomes very important to be able to map between real space, and energy space, to the values of these adiabatic invariants at every stage in model development. The creation of initial conditions, boundary conditions (e.g., Glauert et al., 2018), diffusion matrices (e.g., Horne et al., 2018),

and indeed the calculations within the models themselves (e.g., Loridan et al., 2019) all require mapping between observation space and adiabatic invariant space. The mapping depends acutely on the details of the global magnetic field, and so can be model-dependent. In this paper, we focus on the third adiabatic invariant, L^*, the invariant associated with the drift of the high-energy electron around the Earth. We highlight differences and similarities between L^* calculated using a number of different global magnetic field models. We highlight how a probabilistic model can be used to map observations to computational grid locations in an operational or research-focused radiation belt model in a way that helps to quantify the uncertainty in the relationship.

The Earth's magnetic field is a vast and complex environment, dynamically driven by both internal fields and interactions with solar wind plasma external fields. Although typically in a quiescent state, morphological changes of the magnetic field can be rapid during geomagnetic storms and substorms (Ganushkina et al., 2010; Kubyshkina et al., 2011). Modeling the Earth's magnetic field is therefore a challenging task, and numerous magnetic field models have been introduced, combining mathematical frameworks with both ground and space observations to better describe the magnetic field morphology on timescales of variability (of which the external field can vary from seconds, to hours, days, and beyond the 11-year solar cycle period; e.g., Fairfield & Mead, 1975; Tsyganenko, 1989, 1995, 1996, 2002a, 2002b).

Our ability to perform research within the magnetosphere, to create models and to interpret our findings, hinges crucially on our ability to relate our location in real space to a meaningful position in the Earth's magnetic field. When constructing statistical analyses of datasets, one can use extensive satellite data archives and/or ground-based observing platforms such as magnetometers. Ground observations typically have continuous data-sets with better global coverage, naturally lending themselves to replace satellites in studies when the latter has insufficient data coverage. For example, ground magnetometers in the Canadian Array for Realtime Investigations of Magnetic Activity (CARISMA) contributed to NASA's Time History of Events and Macroscale Interactions during Substorms (THEMIS) mission by investigating macroscale substorm instabilities, storm-time high energy electron production, and solar wind-magnetosphere coupling control mechanisms (Angelopoulos, 2008; Mann et al., 2008; Sibeck & Angelopoulos, 2008).

In this paper, we focus specifically on the relationship between ground-based magnetometer stations and a coordinate set that is appropriate for the study of trapped electrons in Earth's radiation belts. In radiation belt physics the parameter L^* (Roederer, 1970) is a function of the third adiabatic invariant Φ and describes the location of a closed drift path of a charged particle in near-Earth space. This parameter is not a location per se, but it is a useful measure of the behavior of charged particles in Earth's magnetic field and is often used in modeling. Although L^* is not defined on the Earth's surface, ground instruments are used for radiation belt physics through mapping along respective field lines and calculating L^* for equatorially mirroring particles. For example, ULF waves are mapped from ground to space via their footprint locations to infer radial diffusion coefficients dependent on L^* (e.g., Fei et al., 2006; Ozeke et al., 2014, 2012), which inform Fokker-Planck radiation belt models (Roederer & Zhang, 2014). The precise value, or indeed existence, of L^* requires knowledge of the instantaneous global magnetic field configuration across the entire magnetosphere. There are a range of available models, configured for different magnetospheric states and geometries. These can disagree on L^* approximations over a multitude of magnetic latitudes and longitudes (e.g., model comparisons for the last closed drift shell (LCDS) during four events in Albert et al. (2018) (Figures 6–9)). As each model is usually constructed either with a specific set of data or to represent specific magnetospheric conditions, utilizing only one will introduce an inherent bias in the mapped location of the ground observation, which may propagate through the remainder of the study.

In this manuscript, we present Pro-L^*, a freely available probabilistic L^* mapping tool for ground observations to L^* at the magnetic equator. Pro-L^* covers a high resolution grid of ground locations in magnetic latitude, longitude, and magnetic local time (MLT) in the Northern Hemisphere, where the majority of ground instruments are located. Pro-L^* combines multiple magnetic field models probabilistically producing multiple realistic outputs instead of a single value. We specifically embrace the uncertainty inherent in using different magnetic field models to calculate L^*, making an attempt to highlight and quantify it. As L^* is an abstract quantity, it cannot be directly measured and so there is no observed "global truth" with which to compare. Therefore, model produced estimates of L^* would benefit from uncertainty quantification which Pro-L^* provides by design.

The remainder of the manuscript is structured as follows. In Section 2 we explain the method for calculating L^* from a ground location. Section 3 discusses the data which comprises Pro-L^*. Section 4 presents statistical results for each independent magnetic field model from the 11-year data set, and also their combination into a simple probabilistic model for L^*. Section 5 displays usage of Pro-L^* for the Quantitative Assessment of Radiation Belt Modeling (QARBM) 2013 GEM challenge events, with interpolation capability across grid-cells to user-specified locations explored in Section 6. The method for calculating L^*, how to effectively combine magnetic field models into a probabilistic representation, and later developments of Pro-L^* into a functioning model are discussed in Section 7.

2. Computation of L^*

The third adiabatic invariant Φ measures the magnetic flux through drift contours of azimuthally drifting energetic particles trapped in the Earth's magnetic field. Φ is typically conserved for processes occurring on timescales less than the drift period, and is formally expressed as the total magnetic flux enclosed by the drift trajectory

$$\Phi = \int B \cdot d\mathbf{S} \tag{1}$$

where $\boldsymbol{B}$ is the total magnetic field strength and $\mathbf{S}$ is the surface contained within the drift trajectory. The Roederer (1970) L^* is often used as a proxy for distance in adiabatic invariant space, but can be thought of physically as the value which would be equal to the McIlwain L_{m} (McIlwain, 1961) after a "freezing" of the magnetic field and adiabatically turning off all external currents, relaxing to a geomagnetic dipole field (Roederer & Lejosne, 2018). L^* is given by the transformation

$$L^* = 2\pi B_E R_E^2 \,/\, \Phi \tag{2}$$

where B_{E} is the equatorial magnetic field strength at one Earth radii (R_{E}).

The Earth's magnetic field $\boldsymbol{B}$ can be expressed in terms of its internal (I) and external (E) components

$$\boldsymbol{B} = \boldsymbol{B}_I + \boldsymbol{B}_E \tag{3}$$

For all magnetic field models considered in this manuscript we adopt the International Geomagnetic Reference Field (IGRF) internal field model (Finlay et al., 2010; Thébault et al., 2015). The external field is more complicated, and contains contributions from the ring current, $\boldsymbol{B}_{\mathrm{RC}}$, tail current sheet, $\boldsymbol{B}_{\mathrm{TC}}$, large-scale field-aligned current systems, $\boldsymbol{B}_{\mathrm{FAC}}$ (including both Region 1 and 2, see Carter et al., 2016, Figure 1), and the magnetopause currents, $\boldsymbol{B}_{\mathrm{MP}}$ (Tsyganenko, 2013). The total field may therefore be expressed as

$$\boldsymbol{B} = \boldsymbol{B}_I + \boldsymbol{B}_{RC} + \boldsymbol{B}_{TC} + \boldsymbol{B}_{FAC} + \boldsymbol{B}_{MP} \tag{4}$$

The external magnetic field requires models which aim to include some or all of the underlying components, with more advanced empirical models describing the complex geometries with space and ground-based measurements. Since L^* is dependent on the assumed magnetic field model, it is useful to have software containing a range of magnetic field models easily accessible, from which L^* can be determined.

2.1. SpacePy and IRBEM-Lib

SpacePy (Morley et al., 2010) is an open source package in Python, which aims to make data science, modeling and visualizations easier for space sciences (see also Burrell et al., 2018). The package provides a convenient interface to the IRBEM (formally the ONERA) library, a collection of FORTRAN 77 routines for radiation belt modeling, including calculation of magnetic coordinates and drift shells using a range of user-specified magnetic field models (Boscher, 2013).

The IRBEM-Lib calculates L^* via the procedure given in Sections 3.2 and 3.5 of Roederer and Zhang (2014). The second adiabatic invariant J is associated with the bounce motion of trapped particles between magnetic mirror points. Defined as the integral taken along the guiding field line for a complete bounce cycle, in the case of a static magnetic field without field-aligned currents J may be mathematically given as

$$J = 2pI, \quad I = \int_{s_m}^{s_m} \sqrt{1 - B(s) / B_{\mathrm{m}}}\, ds \tag{5}$$

where p is the particle's momentum, I is a line integral function between magnetic mirror points s_{m}, s'_{m} on a given field line, a function of the magnetic field B along the field line and the mirror point field intensity B_{m}. The conservation of J implies that of I. For a specified location and pitch angle, B_{m} is determined and I is calculated by tracing the field line between the two initial conjugate mirror points. To determine the drift shell, points are found at other longitudes where $B = B_{\mathrm{m}}$. Using these points an iterative search is executed to find the field lines with $I_{\mathrm{point}} = I\pm$ some prefixed error. These field lines have an associated footprint on the Northern Hemisphere. If the algorithm fails at a particular longitude, the particle has left its trapping region.

With the located field lines defining the drift shell and their corresponding latitudinal footprints, it suffices to calculate Φ numerically as the magnetic flux through the region on the polar cap Π enclosed by the Northern Hemispheric footprints

$$\Phi = \int_{\pi} \boldsymbol{B} \cdot d\mathbf{S} \tag{6}$$

using the Earth's known surface field B_s in the polar cap (for most models it is sufficient to use a dipole approximation here). With the third invariant calculated, we can therefore obtain L^* using the Roederer (1970) expression. This approach, along with its implementation in SpacePy and IRBEM-Lib, employs several assumptions and limitations which will be explored later in the discussion.

For ground observations, calculation of L^* involves two steps—mapping from the ground station to the magnetic equator, followed by estimating L^* for equatorially mirroring particles at the mapped location. The latter step is therefore a reduced version of the above, since $I = 0$. The same magnetic field model is used in both steps.

3. Data Processing

We seek an L^* database which covers a high enough resolution to sufficiently represent a high proportion of ground observation locations. A significant majority of ground observations are located in the Northern Hemisphere, suggesting that this should be our primary focus. Since there are interhemispheric differences in the ground magnetic field, a separate database should be produced for the Southern Hemisphere. This is a goal of future work. Since a dipole approximation is sufficient for low latitudes, and moderately high latitudes experience mostly open field lines, we focus on magnetic latitudes in Altitude-Adjusted Corrected Geomagnetic (AACGM) coordinates that map to the dipole L range $L = 2.5$–10, with 0.5 L spacing. The choice of uniformity in dipole L rather than magnetic latitude was made to promote a higher density of points at mid-high latitudes, where ground observations are frequently sought. For magnetic longitudes we use a 15° resolution around the Earth from 0°–360°, in order to provide good MLT resolution and capture diurnal variations. The grid is illustrated in Figure 1.

At each gridpoint over the years 2006–2016, hourly equivalent L^* is estimated using seven magnetic field models, outlined in Table 1, chosen for their credibility and relevance to current modeling standards (Olson & Pfitzer, 1974; Ostapenko & Maltsev, 1997; Tsyganenko, 1989, 1995, 1996, 2002a, 2002b; Tsyganenko et al., 2003; Tsyganenko & Sitnov, 2005). For the remainder of this study we will refer to magnetic field models via the model code in Table 1. The earliest of the models is OPQUIET, which unlike the others is analytic. Constructed to take into account the depressed nature of the magnetic field in the inner magnetosphere caused by the presence of the distributed ring current, it well represented currents that flow in a distributed way through a large volume. Initially describing only the symmetric component of the magnetosphere, the model was later developed to include dipole-tilt effects. These significant limitations are balanced by the

property that the OPQUIET model can always provide a value for the magnetic field and does not require input data that may be lacking from the monitoring record or in real-time.

As time progressed, magnetic field models evolved from analytic approaches to incorporate satellite data and more sophisticated parameterization. T89 was among the first, constructing a simple empirical approximation for the global magnetosphere, binned into several intervals of the geomagnetic disturbance index Kp. The model incorporated a thin current sheet with two-dimensional warping near the inner edge of the plasma sheet in the nightside which plays a key role in the dynamics of disturbances, since it is at the boundary between the internal field sources and the magnetotail currents. Since a simple parameterization by Kp combined a collection of physical processes together, it was recognized that the current solar wind state might add more information to the parameterization. T96 adopted this approach and developed on the T89 model, explicitly defining a realistic magnetopause, large-scale Regions 1 and 2 Birkeland current systems, and interplanetary magnetic field (IMF) penetration across the boundary. The nature of subsequent Tsyganenko models prior to 2016 was to update and expand on previous models. T01QUIET updated the approaches given in T96, introduced a partial ring current, and included integrals of geoeffective IMF-related parameters with hourly time history into the model parameterization. T01STORM configured T01QUIET for a set of rare geomagnetic storms, taking into account the nonlinear response of the magnetosphere to abnormally strong disturbances in solar wind, which previous models ignored. T05 recognized that different sources of the geomagnetic field have different response and decay times, which was overlooked in T01STORM, and introduced terms in the model parameterization to account for these response and decay times. The most recent Tsyganenko models fit the magnetic fields using basis functions and no longer use parameterized representations of current systems (see Tsyganenko & Andreeva, 2016, 2017). These models are currently not available in SpacePy and therefore not included in Pro-L^*.

The final model we use to construct Pro-L^* is OSTA, which is parameterized by solar wind properties yet independent of the Tsyganenko models. Using a database of more than 14,000 magnetic measurements by Fairfield et al. (1994), the statistical connection between the external field, satellite data and geomagnetic indices was explored, resulting in a magnetic field with dipolar azimuthal symmetry, with additive day-night asymmetry and dipole-tilt effects. Further models relevant to this study exist, but are not available in our chosen software. Incorporation of more recent models (Tsyganenko or otherwise) is a goal of future development. Some models are more suitable for quiet or storm times, and many of the Tsyganenko family of models are developments of previous versions. In this work, we assume that all magnetic field models are independent and therefore contribute equally to our L^* estimate. We discuss comparisons between the models, validity and weightings later.

In addition to L^*, for each magnetic field model we also store the McIlwain (1961) L_m, equatorial magnetic field amplitude $\boldsymbol{B}$, and geographic Cartesian location $\mathbf{x}$ at the point on the magnetic equator mapped from each ground location. These variables are also stored for the case of no external magnetic field, that is, purely the IGRF. The MLT of each gridpoint is also stored. Collecting these variables hourly for each gridpoint over 11-year results in Pro-L^* containing approximately ~1.9 billion entries. L^* calculations alone account for ~ 260 million. Creating the database is a very computationally expensive task. Calculating L^* for a single hour, across all seven models and the full grid, takes approximately 13 h on a single core. The total number of CPU hours used in calculating the data set is in the vicinity of 127,000. Although parallelization of L^* calculations across multiple cores has drastically reduced the database formulation time to the order of weeks, it is clear that the mapping of ground-based data and calculation of adiabatic coordinates is unreasonably expensive. A key benefit of Pro-L^* as a statistical model for radiation belt applications is that calculations need only to be executed once; any subsequent statistical results can be derived from Pro-L^* on timescales much shorter than manual computation.

4. Statistical Results

In this section, we present individual model statistics deduced from Pro-L^*, and demonstrate a simple approach to combining all models into probabilistic models. These models allow for an extensive statistical study in multidimensional space, and we present key results in this manuscript. Further relevant results are provided in the Supporting Information.

4.1. Individual Model Statistics

Global L^* median and interquartile range (IQR) maps for each magnetic field model are shown in Figures 2 and 3. Each plot depicts a polar projection of our grid looking down on the magnetic North Pole. Magnetic latitude decreases radially from the center and MLT extends anticlockwise from midnight at the rightmost point (an imaginary Sun is to the left of each diagram). However, since we are mapping these ground locations to the magnetic minimum in space along the same field line, we choose to indicate the equivalent dipole L value on each plot, rather than magnetic latitude (remember that our grid is uniformly spaced in equivalent dipole L, not magnetic latitude). Note that the equivalent dipole L decreases from the pole outwards in the plot.

White regions in each radial plot indicate the absence of any mapped L^* estimates at that grid location. To accompany Figures 2 and 3, occurrence maps with the same plot format for each magnetic field model are shown in Figure 4, to demonstrate the occurrence of successful L^* estimates in all regions. Note that we assume that where the L^* calculation fails, it does so because that ground location does not map to a closed drift path. This could be because (a) there is no equivalent closed drift path at the mapped location for a 90° pitch-angle electron; or (b) the L^* determination was not completed due to constraints in the IRBEMlib calculation ($L_m > 10$ for all models, or if the $x < -15R_E$ in geocentric solar magnetospheric coordinates for T05). All input variable data for the empirical magnetic field models contain no gaps (with interpolation performed as in Qin et al., 2007) and is not a cause for model default.

As expected, almost all models fail to provide L^* values on the nightside at high latitudes. L^* values begin to fail on the dawn and dusk flanks at the highest latitudes, and only succeed at lower latitudes closer to midnight. Coverage for all Tsyganenko models remains fairly consistent, but T01STORM has the best coverage suggesting that T01STORM provides storm-time configurations that support closed drift paths at higher latitudes. Conversely, OSTA has full global coverage and is defined for both quiet and disturbed times. This model should be used with caution, however, since median L^* values at high latitudes on the nightside do not monotonically increase with latitude and are therefore unphysical.

We should note that a failure to calculate L^* is not a failure of the magnetic field model and instead reflects the fact that L^* is only defined on a closed drift path. We do not expect our chosen ground-based grid to map to valid L^* on the entirety of the nightside, because high latitude stations map to open-field lines, or to regions of the magnetosphere just inside the open-closed field line boundary, that may not support closed drift paths. Where multiple magnetic field models produce an L^* value at the same location is a good indication of where L^* truly exists. When only one model produces an estimate of L^*, it suggests that we should be less confident in the estimate. We discuss in Section 4.2 methods for combining results from multiple magnetic field models.

All magnetic field models exhibit similar median L^* spatial profiles. The dayside has full coverage of L^*, increasing steadily in magnetic latitude with the compressed field lines at noon, attaining its maximum at the highest latitude. As we extend round the dawn-dusk flanks, the location of maximum L^* values fall to lower latitudes. This day-night asymmetry is not surprising due to the nature of field line compressions, stretching and reconnections throughout the Dungey cycle. More recent models tend to estimate larger values of L^* values from dusk through midnight to dawn. There is a small patch of low L^* estimates at high latitude on the nightside in the T05 model, which are also likely to be unphysical.

Differences appear between models once we consider the IQR of the estimated L^*. Generally speaking, L^* estimates are highly reproducible in all magnetic field models for all latitudes below 60° ($L_{dip} = 4$). Here, IQR values are less than 0.1. This is unsurprising as we expect the internal magnetic field to dominate at lower latitudes. As expected, the early OPQUIET model has the least variability over all latitudes. It should be stressed however that a model with low variability does not suggest an accurate model. The magnetosphere is a very dynamic environment, and variability in L^* should be anticipated. All other models exhibit bell-shaped regions of heightened uncertainty, somewhat symmetric through the noon-midnight plane. These regions extend from around 66° ($L_{dip} = 6$) to the highest latitude on the dayside, and from 60° ($L_{dip} = 4$) to the L^*-definition boundary on the nightside. Although successive Tsyganenko models partially reduce the extent of the uncertainty region on the dayside, the nightside region remains considerably variable, with IQR ~ 1. This is likely the result of changing conditions in the magnetic field due to the solar wind

and geomagnetic activity being more prevalent at high latitudes on the nightside. The T01STORM and T05 models, which were configured to geomagnetic storms, also show enhanced variability during predawn at higher latitudes. In all models the quantified uncertainties in the bell-shaped regions are large enough from a modeling perspective to justify that a probabilistic L^* is necessary.

The shape of model distributions in each MLT sector (dawn [3–9], noon [9–15], dusk [15–21], and midnight [21–23]) for a selection of magnetic latitudes is shown in Figure 5. The remainder of magnetic latitudes studied are provided in the Supporting Information. In all MLT sectors L^* displays little variability at the lowest latitude, with variability small enough to appear almost as a delta function when viewed on the same scale as the other latitudes. As magnetic latitude increases, the analytic OPQUIET model quickly breaks from the empirical models across all MLT sectors and does not resemble the shape of any well-known distribution. Concurrently at dawn and dusk, the remaining distributions of L^* display increasing variability as latitude increases. The distributions are quite positively skewed at 66.91° and 67.79°, before becoming increasingly Gaussian at 71.57°. Comparing between the Tsyganenko family of models, the Gaussian profile becomes smoother progressively with each successive model release. At noon, the distribution of L^* also displays increasing variability with increasing latitude, but the distributions are negatively skewed for 66.91° and 67.79°, before becoming more Gaussian at 71.57°. Comparisons between model distributions of L^* are unfair for high latitudes in the midnight sector because not all models return L^* values in this region. However, it is surprising that the shapes of the midnight distributions at 66.91° are similar to those at the highest latitude in all other sectors.

The distributions demonstrate that constructing models of variability in L^* is a complex problem since we have multiple sources of uncertainty. In our probabilistic model, it is imperative to distinguish when variability in our L^* estimate represents variability in the true L^* value. In some regions the variability in our L^* estimates is magnetic field model dependent. At other locations where L^* distributions are roughly the same for all magnetic field models, any variability in our L^* estimate is mainly due to changing conditions in the magnetosphere which are correctly captured using our magnetic field models. We must both identify and treat these as distinct sources of uncertainty.

4.2. Simple Global Probabilistic L^* Models

The most simple approach for combining colocated L^* values calculated by individual magnetic field models is to equally weight the L^* estimate from each magnetic field model and provide the median. This is the most straightforward approach, but each model used in our study is not fully independent. For example, on a technical level each Tsyganenko model is a development on the one preceding it, and we expect each successive model to provide a better description of the magnetic field geometry and thus hold more weight in a probabilistic model. It must also be stressed that determining when L^* is not physically defined is as important as accurately calculating its value when it is. Combining models in a simple equally weighted averaging approach would combine NaN values (i.e., no L^* defined at this time for this ground-based location) with finite values in a way that could prove to be misleading.

Instead, we define confidence in L^* (both the existence of L^* and the estimated value) as the number of models that return a value. Then, we can naively combine the finite values of L^* in a simple way to investigate how model uncertainty might affect the distribution of L^*. Contour maps for the median, IQR, and occurrence regions of the global probabilistic models are illustrated in Figure 6. Each probabilistic model is described by the threshold confidence value m—the number of magnetic field models required to return an L^* value at any given time. From Figure 6, we immediately observe that a confidence level of at least $m = 3$ is necessary to obtain physical (monotonically increasing with latitude) L^* distributions on the nightside. Assuming that $m = 3$ is satisfactory for estimating L^* from combined model outputs, it may be sensible to assume that L^* is always undefined for ground locations beyond the vicinity of 68° ($L_{\mathrm{dip}} = 7$) on the nightside. As we trace through predawn and postdusk, the definition boundary, the latitudinal boundary between defined and undefined L^*, increases smoothly until L^* is fully defined at dawn and dusk. As we increase the number of models required the L^* definition boundary erodes to lower latitudes. Note that we can only infer this boundary from our calculations at discrete locations in magnetic latitude. We do not expect the true latitudinal boundary for L^* existence, analogous to the LCDS, to exist precisely at one of our grid locations.

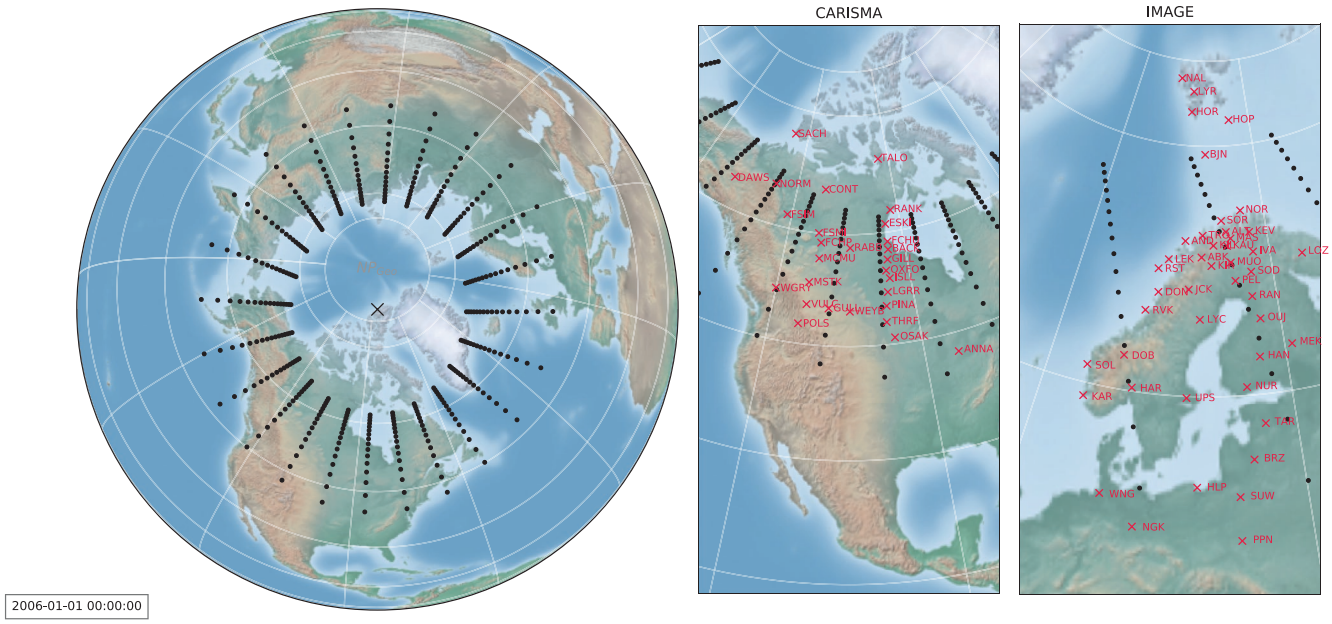

Figure 1. A snapshot of January 1, 2006 showing (left) the Pro-L^* spatial domain in AACGM coordinates projected down onto the magnetic North Pole (x), as well as onto two popular magnetometer arrays: CARISMA (center) and International Monitor for Auroral Geomagnetic Effects (IMAGE, right). The associated geographic locations of the magnetic coordinates will vary with time. AACGM, Altitude-Adjusted Corrected Geomagnetic; CARISMA, Canadian Array for Realtime Investigations of Magnetic Activity.

The largest values of L^* exist in small bands close to the definition boundary. For $m = 3$, the largest values fall between $10 < L^* < 11$, from dusk to dawn. As m increases, the median value of L^* close to the L^* definition boundary reduces, largely because the location of the boundary is eroded to lower latitude. The spatial distribution of L^* on the dayside appears stable regardless of m, with L^* defined at all latitudes and very little reduction in IQR as m increases. Increasing m reduces the extent of the region of large IQR on the flanks and at midnight, but again this is largely because the L^* definition boundary is eroded to lower latitude. Across the nightside magnetosphere from dusk until dawn, the IQRs in the region of highest L^* values remain in the vicinity of 1, even with the model number threshold at its highest. It is interesting to note that the median L^* values observed at the highest latitude at noon are around $2L^*$ smaller than those seen at the definition boundary at midnight, with similar variability. This suggests the ability to explore dynamics on the nightside over a considerably larger range of L^* than the dayside, but for ground stations only spanning mid-low latitudes.

Figure 7 shows probability density function (PDF) estimates for L^* at 67.79° ($L_{dip} = 7$) as a function of m and MLT sector, notable as the typical latitude of the L^* definition boundary for the majority of magnetic field models on the nightside. Each PDF estimate was found using kernel density estimation (KDE) with a Gaussian kernel and Scott's rule (Scott, 1979) to determine the bandwidth (see Haiducek et al., 2020; Morley et al., 2018; Watt et al., 2019 for other examples of KDE usage in space physics). Similar figures containing all magnetic latitudes can be found in the Supporting Information.

The effects of increasing m shown in Figure 7 are representative of all latitudes above 64.76° ($L_{dip} = 5.5$), with the exception of the midnight sector where distributions break down beyond 67.79° and should be used cautiously. At latitudes below this, the addition of further models appears to have minimal influence on the shape or variability of the resulting distributions, most likely due to the dominance of the internal IGRF field. Nevertheless, the noon sector appears resilient to increasing m even at higher latitudes, with only a slight decrease in variability at the inner edge of the distribution when we require an L^* output from all magnetic field models. Dawn and dusk exhibit multimodal distributions. Increasing m significantly reduces variability in the tail of the distribution (and slightly at the inner edge). Reductions in variability (about $1L^*$ from the lowest to highest m value) make peaks in the heart of the distributions more prominent, although they are well defined by $m = 3$. The multimodal nature of the distributions are unsurprising when

Table 1
Magnetic Field Models Used for L Calculations*

Code	Citation	Quiet/storm	Model parameters
OPQUIET	Olson and Pfitzer (1974)	Quiet	Analytic
T89	Tsyganenko (1989)	Both	Kp
T96	Tsyganenko (1995, 1996)	Both	Pdyn[a], Dst, B_y-IMF, B_z-IMF
OSTA	Ostapenko and Maltsev (1997)	Both	Pdyn, Dst, B_z-IMF, Kp
T01QUIET	Tsyganenko (2002a, 2002b)	Quiet	Pdyn, Dst, B_y-IMF, B_z-IMF, G1[b], G2[b]
T01STORM	Tsyganenko et al. (2003)	Storm	Pdyn, Dst, B_y-IMF, B_z-IMF, G2[b], G3[b]
T05	Tsyganenko and Sitnov (2005)	Storm	Pdyn, Dst, B_y-IMF, B_z-IMF, W1-W6[c]

[a]Pdyn—Solar wind dynamic pressure. [b]G#—Integrals of geoeffective interplanetary magnetic field (IMF)-related parameters over the preceding 1-h interval. [c]W#—G# plus further terms to include response and decay times exceeding 1-h.

we view the changes in dawn and dusk median L^* values at high latitudes in Figure 2, suggesting higher MLT resolution of L^* is required in these regions for more accurate modeling. In the midnight sector increasing m drastically reduces both variability and the distribution center. This is a direct result of model variability becoming more dominant over physical variability with increasing latitude, which does not seem to occur in other MLT sectors. In all MLT sectors, it is important to remember that a reduction in variability is not indicative of more accurate modeling. On the surface, requiring that more models return a L^* is likely to remove any real physical variability gained from the inclusion of current systems not shared between all models (although this is more complex due to the different ways in which magnetic field models are built—see Section 7). Choosing m is a trade-off between avoiding model bias and preserving the underlying physical variability of the system.

Creating the probabilistic models illustrated here was a simple attempt to reduce some of the uncertainty between magnetic field model configurations. We did not address any of the variability due to changing physical conditions, however, other than those physical processes which might be gained by the addition of particular current systems in more sophisticated magnetic field models. Most observed times are quiescent which dominate the L^* distributions, and results shown might not be indicative during times with enhanced activity. A natural next step would be to separate L^* distributions further, in the more simple case between quiet and storm phases, to investigate whether variability due to changing conditions is significant.

Since Pro-L^* contains a wealth of calculated L^* values it is also a useful tool to look at individual test cases which might have unique or well-defined properties. In these scenarios we are able to compare performance of individual magnetic field models against probabilistic techniques, illuminating benefits that a probabilistic model can yield over an arbitrary choice of a singular magnetic field model.

5. Case Study: 2013 GEM Challenge Events

A great deal of magnetospheric research uses select ground instruments to track and measure physical quantities over continuous periods of time. These may provide insight into global responses to geomagnetic storms (e.g., Xu et al., 2017) and substorms (e.g., Forsyth et al., 2015; Orr et al., 2019), as well as supplying evidence of expected phenomena such as magnetic pulsations (e.g., C. P. Wang et al., 2018). It is therefore important to see how L^* varies with ground location over time, in addition to statistical MLT variation, to relate these ground observations to adiabatic locations in space for radiation belt studies. However, classical approaches require a decision for which magnetic field model to use, or an assumption for L^* must be made (ie. a dipole), which we have shown brings inherent uncertainty. Here, we demonstrate usage of Pro-L^* as a probabilistic alternative to reduce model selection systematic biases, for four events in 2013 which comprise the radiation belt challenge set by the QARBM focus group within the GEM program (Tu et al., 2019). For each of the events we consider four grid locations in the vicinity of four popular ground magnetometer sta-

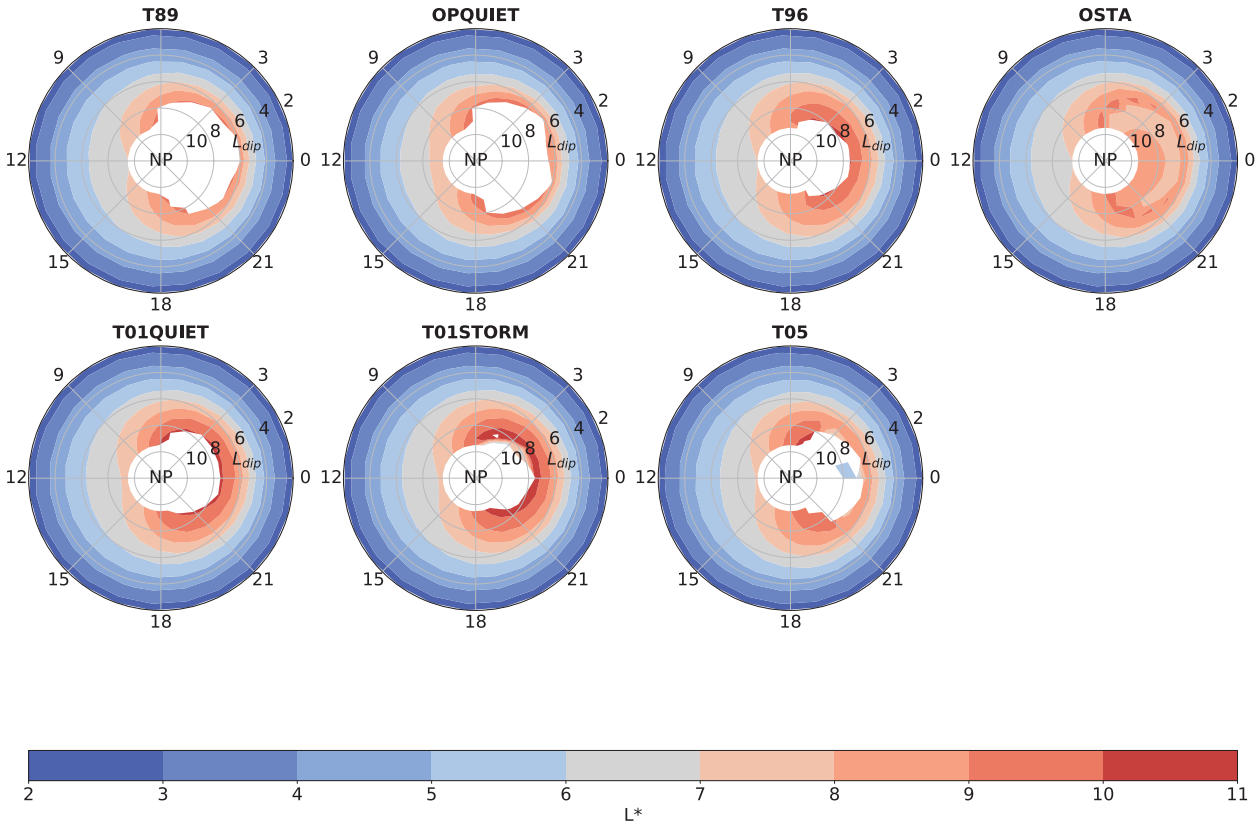

Figure 2. Global median L^* maps shown for each magnetic field model. The maps are displayed in MLT and dipole L, projected onto the magnetic North Pole with the Sun to the left. Magnetic latitudes have been converted to dipole L for display purposes. Codes for each model are as in Table 1. MLT, magnetic local time.

tions in the CARISMA array at around 330° magnetic longitude: Pinawa (PINA), Island Lake (ISLL), Gillam (GILL), and Fort Churchill (FCHU). A summary of the four events is as follows:

- **March 17, 2013 through March 19, 2013 Storm Enhancement**: A strong acceleration event on March 17 and 18 following a coronal mass ejection impact on March 17. Beginning around 8:00 UT on 17 March, there was a period of 18 h of continuous southward IMF B_z. During this time there was considerable substorm activity, indicated by the elevated Auroral Electrojet Index. This was a moderately strong storm with a minimum Dst index of 130 nT (e.g., Boyd et al., 2014; Hudson et al., 2015; Z. Li et al., 2015; W. Li et al., 2014; Ma et al., 2018; Olifer et al., 2018; Shprits et al., 2015; Ukhorskiy et al., 2015; C. Wang et al., 2017; Xiao et al., 2014).
- **May 31, 2013 through June 3, 2013 Storm Dropout**: Characterized by a minimum Dst of −119 nT on June 1, 2013, strong MeV electrons before and after the storm were recorded with a clear, nonadiabatic main phase dropout (e.g., Clilverd et al., 2015; Kang et al., 2018).
- **September 19, 2013 through September 21, 2013 Nonstorm Enhancement**: Identified on September 19–20, 2013, with a minimum Dst of −19 nT. No storm like profile, but some substorm activity (e.g., Ma et al., 2018; Pakhotin et al., 2014).
- **September 23, 2013 through September 26, 2013 Nonstorm Dropout**: Recorded on September 24, 2013 with a minimum Dst of −22 nT. Yet, there was not a classic storm profile in Dst accompanying the rapid depletion in MeV electron responses (e.g., Capannolo et al., 2018; Pakhotin et al., 2014; Su et al., 2016).

We present here the results for the storm time dropout and enhancement, respectively, in Figures 8 and 9, with the remaining two events provided in the Supporting Information. The results for the nonstorm events are similar to their storm counterparts, but of a smaller magnitude and with little variation at lower

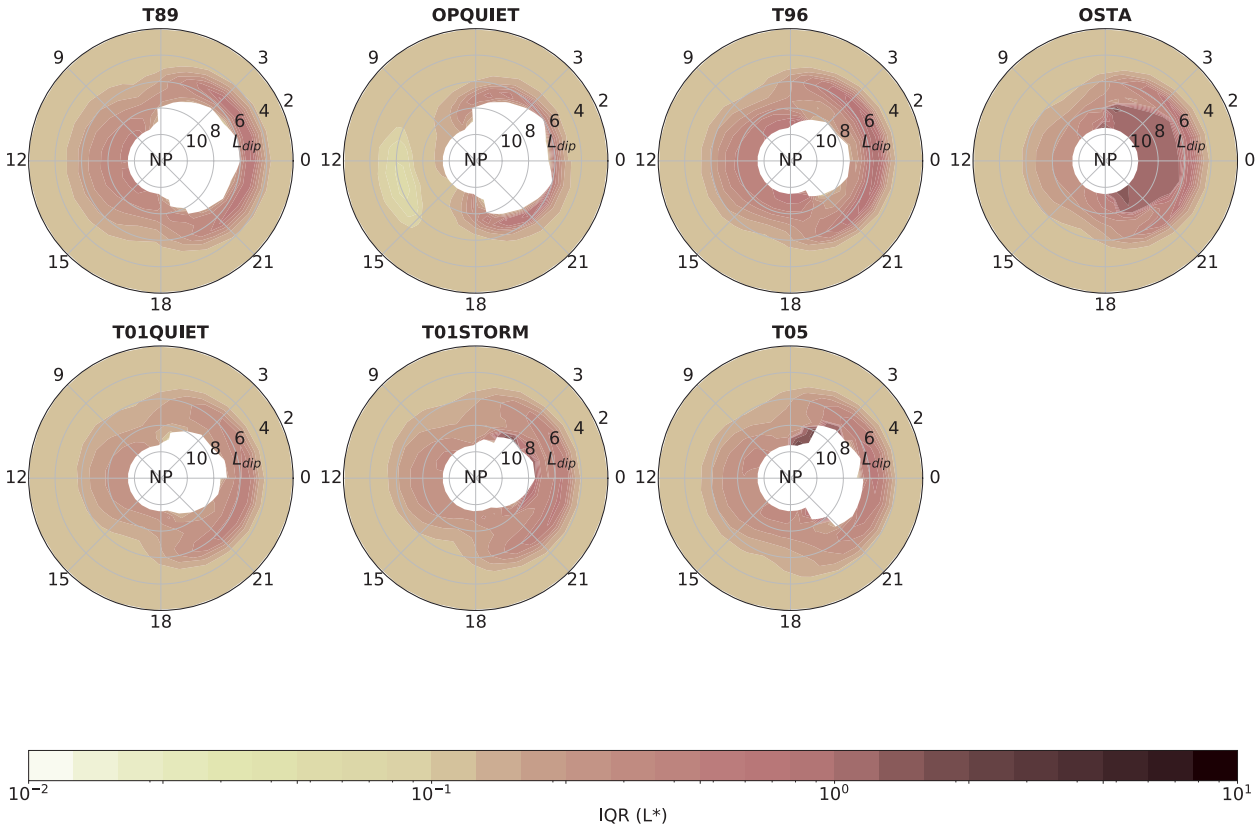

Figure 3. Global L^* IQR maps shown for each magnetic field model. Each figure follows the same format at Figure 2. Codes for each model are as in Table 1. IQR, interquartile range.

latitudes. In the figures, the bottom four panels display L^* outputs for all magnetic field models at each considered latitude, increasing in latitude as we travel down the panels. Each L^* output is normalized by its respective constant dipole approximation at that particular magnetic latitude, so that variation at different latitudes can be considered on a similar scale. We have also included a median L^* subject to the requirement that at least three magnetic field models return an L^* value (a subset of values from our threshold = 3 probabilistic model). Each panel time series covers a period which spans the particular event plus/minus a day and a half. The Dst and Kp indices are also shown for the entire period in the top panel.

In Figure 8, we observe that there is an immediate response to the enhancement at all latitudes, characterized by a sharp drop in Dst and heightened Kp, for all magnetic field models. The event begins while our ground locations of interest are on the nightside, and most of the magnetic field models immediately appear to indicate open drift paths at much lower latitudes than expected at quiet times. While a significant proportion of models produce an L^* output at the lowest latitude, the variability between models is significant compared to the rest of the time series and persists throughout the main phase of the storm. During the enhancement, all empirical models predict an L^* which is significantly larger (where L^* is not undefined) than that given by a simple dipole approximation or the OPQUIET model on the nightside, and significantly less on the dayside. This clustering of the empirical models appears to be stronger on the dayside. Model variability extends throughout the recovery phase, still visibly apparent 1.5 days after event onset, with lower latitudes stabilizing faster. However, the absence of a storm does not guarantee a constant magnetospheric state, as there are diurnal variations between day and night. The empirical magnetic field models disagree on the nightside preceding enhancement, although this is definitely exacerbated during the storm commencement. This re-emphasises that a simple storm/quiet L^* probabilistic model may not be sufficient since variability can occur at all times, even in the absence of heightened geomagnetic activity.

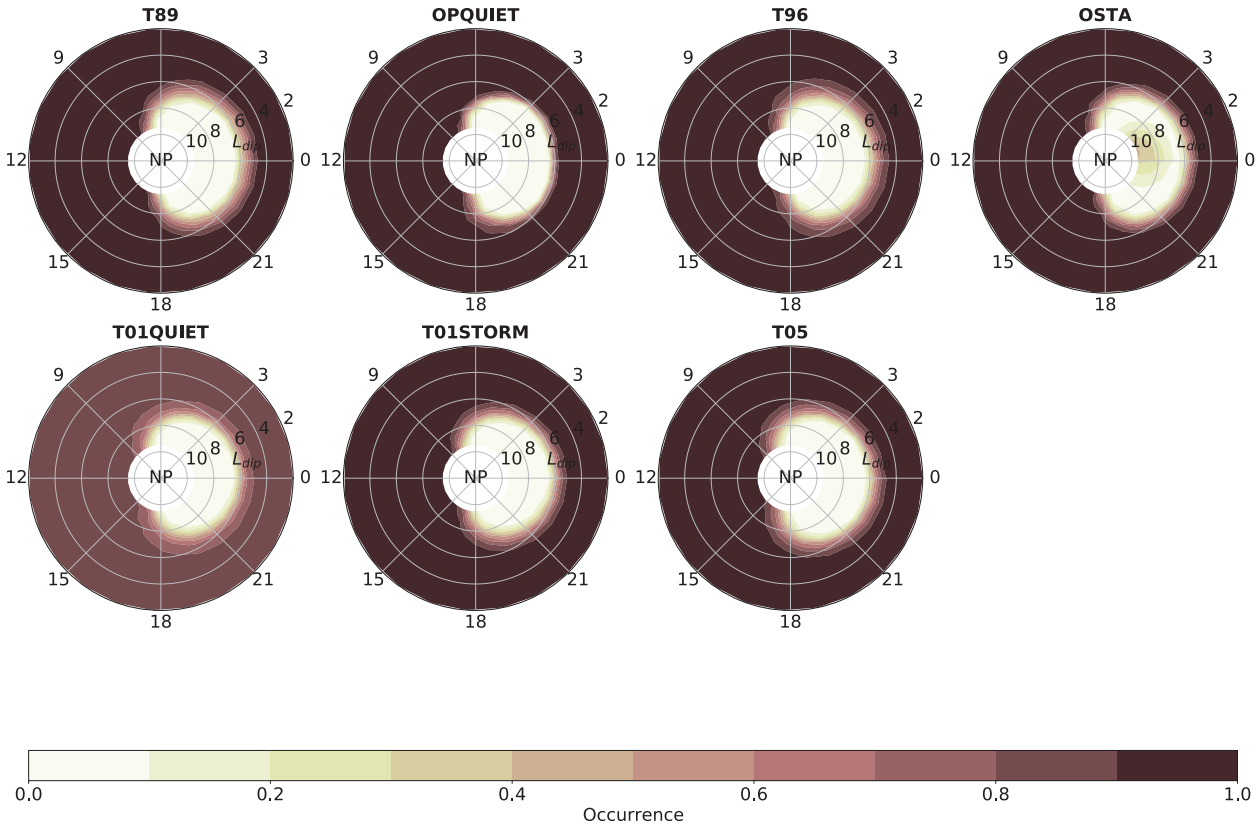

Figure 4. Global occurrence maps for a defined L^* shown for each magnetic field model. Each figure follows the same format at Figure 2. The occurrence values were calculated as the ratio between the number of L^* values returned to the total number of observations (L^* defined and undefined) in each bin. Codes for each model are as in Table 1.

The behaviors of the magnetic field models preceding the storm, during enhancement onset, and extending into the recovery phase are generally the same as for the dropout event. However, the immediate default of magnetic field models to open-drift paths at dropout onset appears to penetrate deeper to lower latitudes, with most models defaulting at all latitudes except the lowest. By the recovery phase, the boundary for closed drift paths on the nightside has retreated slightly but still penetrates deep into the mid-latitudes. The only models with reasonable coverage at onset for all magnetic latitudes are the analytic OPQUIET quiet-time model, which is not valid for storms or the nightside, and the empirical OSTA model. Remarkably, the latter reverses the standard diurnal variation in L^* approximations at dropout onset, re-emphasising that this model should be used with vigilance when it is the only empirical model returning an output. The pre-dropout variability is also different to the pre-enhancement variability on the nightside. Prior to the dropout, the empirical models post-T89 are well clustered, with nightside variability predominantly due to the analytic and aforementioned T89 models. Since these models are the eldest we anticipate they are likely to be most inaccurate. Therefore, the clustering of the other empirical models in the nightside suggests that the possibility of a more stable L^* structure in this region, spanning multiple latitudes, generally exists.

In both test cases the median L^* based on the model threshold follows the clustering of magnetic field models, and is therefore likely to be more representative of the *best estimate* of L^*. The model also defaults in regions where we would expect and highlights structure within the variable regions that can be easily compared to the quiescent diurnal variations. Model uncertainty during both storm and nonstorm events is profound, and decisions to simply use a singular magnetic field model can immediately introduce large uncertainty in the associated adiabatic location, which progresses through all remaining analysis (e.g., Loridan et al., 2019). Since a probabilistic model offsets some of the outlier model bias the benefits are immediate.

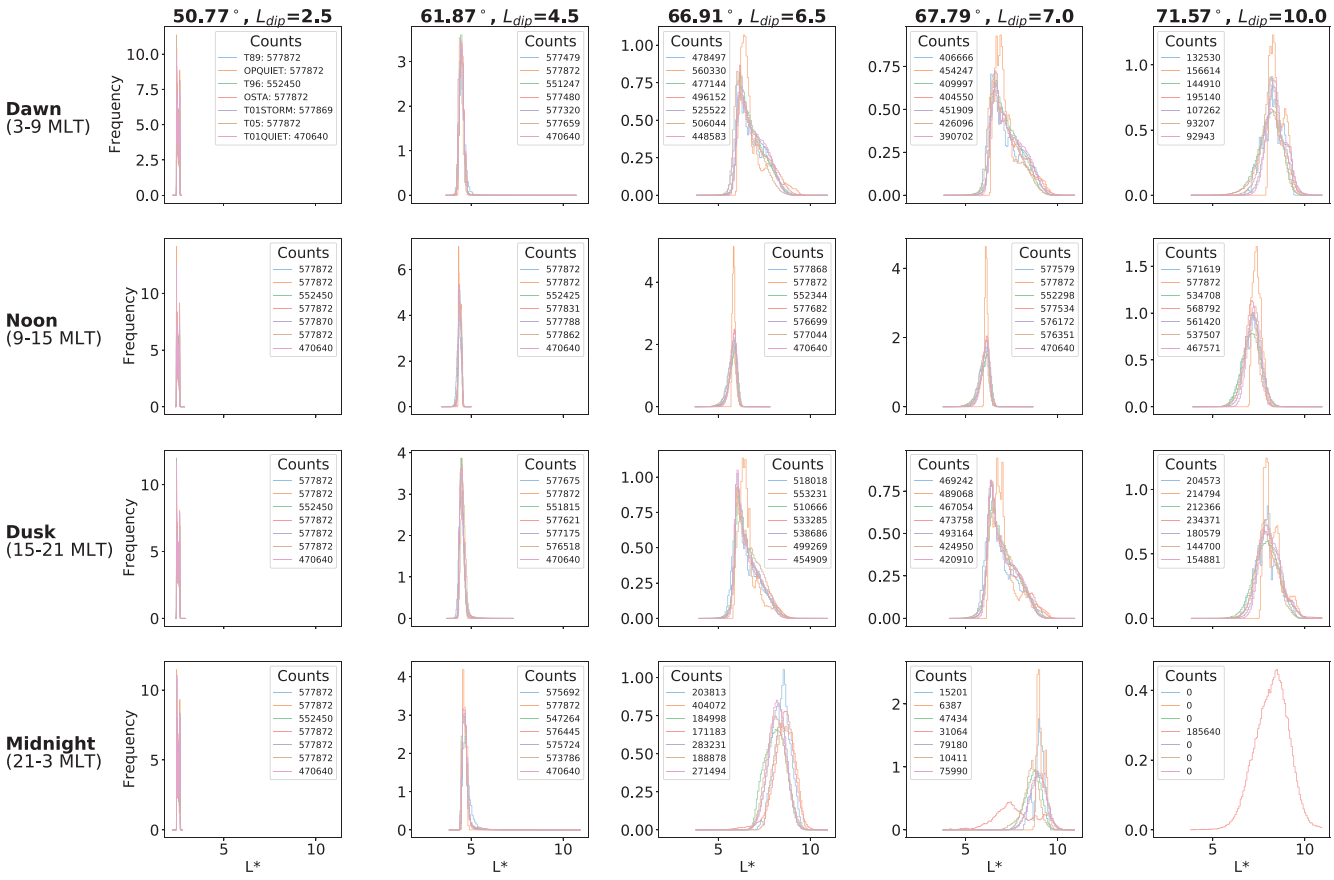

Figure 5. Step-histograms for each magnetic field model, shown for a selection of magnetic latitudes and separated into MLT sectors. The number of bins is 100 for all histograms, with bin locations identical over all MLT sectors for each magnetic latitude. Occurrences of defaulting L^* calculations are not taken into consideration. MLT, magnetic local time.

6. Grid Interpolation

The L^* time series produced from a probabilistic model are useful for researchers using magnetometers off-grid to Pro-L^*. Our static geomagnetic grid used for Pro-L^* was chosen to give uniform global coverage, focusing on areas in the Northern Hemisphere where ground instruments are generally located, but with not such a high resolution as to demand unfeasible computing costs. These choices mean that the gridpoints in Pro-L^* will not line up exactly with the coordinates of several ground instruments. Making the best use of magnetic field measurement output combinations, we can formulate a realistic global L^* manifold on which interpolation between locations may be possible. In this case, calculating L^* for any ground magnetometer would be simple with quantified uncertainty (i.e., IQR) and avoids the computationally demanding process of calculating L^* directly. For successful usage of Pro-L^* in real world applications, it is important to know when and how L^* values can be interpolated across gridpoints to ground instruments of interest. In Figures 10 and 11, we show the latitudinal and longitudinal changes in median L^* from the Pro-L^* model across the four different events displayed in Section 5. These figures help to demonstrate visually when and where interpolation between gridpoints would be appropriate. There are two points to consider when making interpolations. First, the physical definition of L^* does not hold if it is not monotonically increasing with magnetic latitude. Second, there appears to be a diurnal variation through day and night, with pivots for increases and decreases in L^* occurring at midnight and midday, respectively. This can act as an indicator for reliable interpolation across magnetic longitude. During dropouts and enhancements the second criteria may break down, but this does not necessarily mean that interpolation should be avoided.

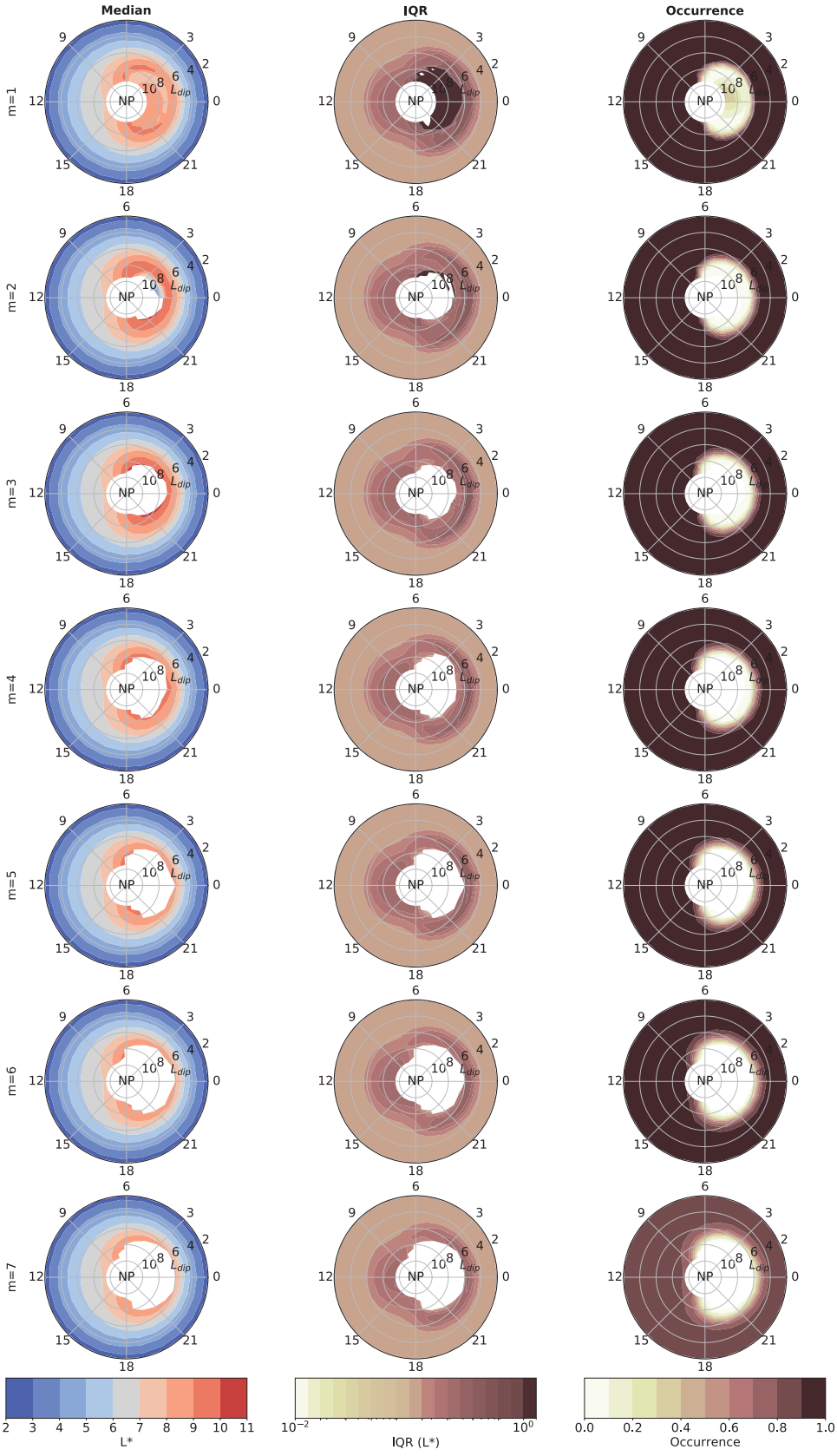
Median
IQR
Occurrence
m=1
m=2
m=3
m=4
m=5
m=6
m=7
NP
L*
IQR (L*)
Occurrence

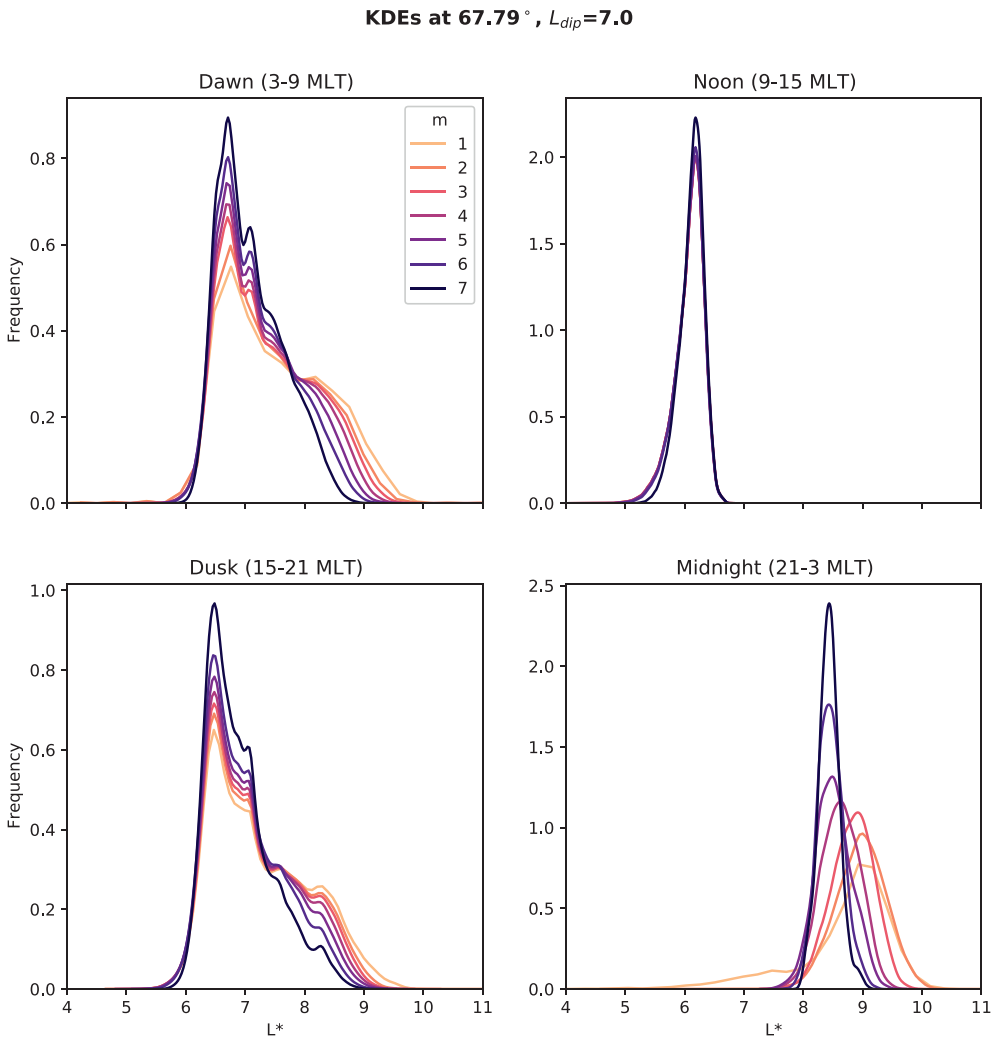

Figure 7. KDEs of global probabilistic L^* models at 67.79° magnetic latitude ($L_{dip} = 7$) separated into MLT sector. The KDEs are shown as a function of the model threshold number m. MLT, magnetic local time; KDE, kernel density estimation.

Figure 10 shows the northward latitudinal changes in L^*, with respect to magnetic latitudes in the Pro-L^* domain, for the four 2013 GEM challenge events at 330° magnetic longitude. Here, L^* is the median of all magnetic field outputs provided that at least three magnetic field models to provide an L^* output (else L^* is assumed to be undefined). For each event we have also shown the boundary for monotonic increases, indicating where L^* no longer has physical meaning. In quiescent times there is a clear boundary which follows a periodic diurnal variation with MLT. At midnight the boundary typically sits around 66.9° but is very sensitive to enhancements in geomagnetic activity which pushes the L^* definition boundary to lower latitudes. At noon we appear to always have full interpolation capability in quiescent times. During geomagnetically active events we see that this periodic structure immediately breaks down. Interpolation throughout dawn, noon, and dusk appears mostly resilient to event dynamics, except for the storm enhancement. At midnight we see an immediate response to the event onset with significant latitudinal decreases of the interpolation boundary, which is pushed lower for storm events than nonstorm. In fact, distortion of the boundary for nonstorm events is not too dramatic, and interpolation is possible with larger confidence.

Figure 6. Global L^* median (left) and IQR (center) maps as a function of m models determining the existence of L^* at any given time. Occurrence maps (right) for each value of m are also shown. Each figure follows the same format at Figure 2. IQR, interquartile range.

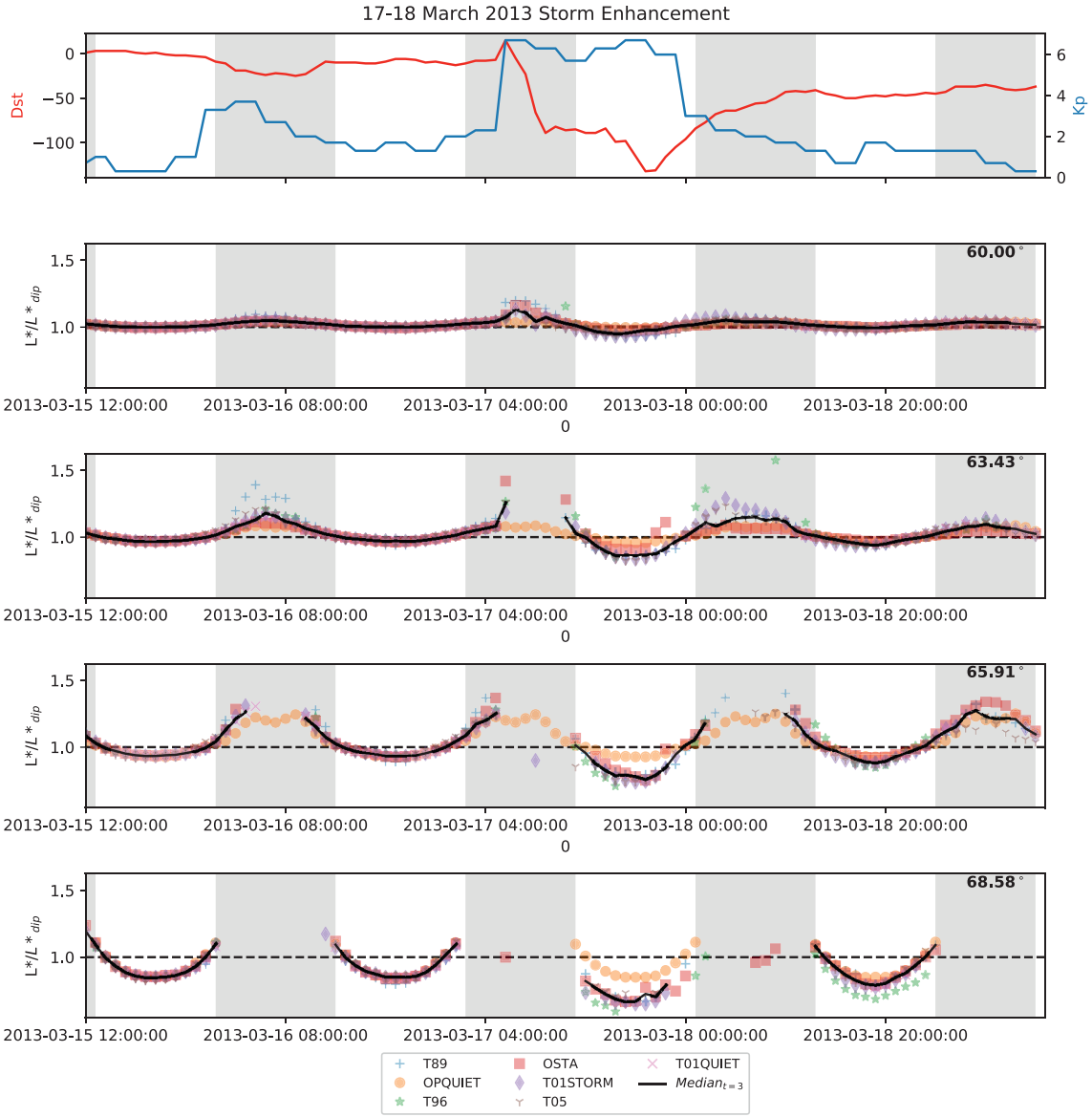

Figure 8. The response of L^* magnetic field models to the March 17–18, 2013 storm enhancement, for a selection of magnetic latitudes at 330° magnetic longitude, where ground observations are frequently of interest. The median L^* is also given provided that at least three magnetic field models return a L^* value. All returned L^* are normalized by their respective constant dipole approximation for comparison of latitudes on the same scale. The Dst and Kp indices are also provided over the given time period. Shaded bars indicate times where observed values are on the nightside.

Figure 11 shows the eastwards longitudinal change in L^*, for the four 2013 GEM challenge events at the magnetic latitudes used for the test cases in Section 5. L^* is again defined as in Figure 10 and approximate locations of midday and midnight have been indicated by black-dot and pink-dot markers, respectively. The expected diurnal variation can be seen both for individual longitudes as they progress through time as well as across longitudes in a single time instance. Surprisingly, this structure weakens with decreasing magnetic latitude, with longitudinal changes in L^* more oscillatory at the lowest latitude. However, the oscillating changes are small in magnitude. The smoothness in interpolation is highly sensitive to both enhanced geomagnetic activity and magnetic latitude, with disruptions seen clearly at relatively low latitudes in both storm and non-storm events. Shortly after event onset the general structure of diurnal variation is largely unaffected at the lowest latitude, yet disrupted at all other latitudes (excluding the nonstorm enhancement at 63.43°) with either more intense changes in L^* between successive longitudes or L^* no longer being defined over varying regions across the nightside. During these instances, we should approach interpolation

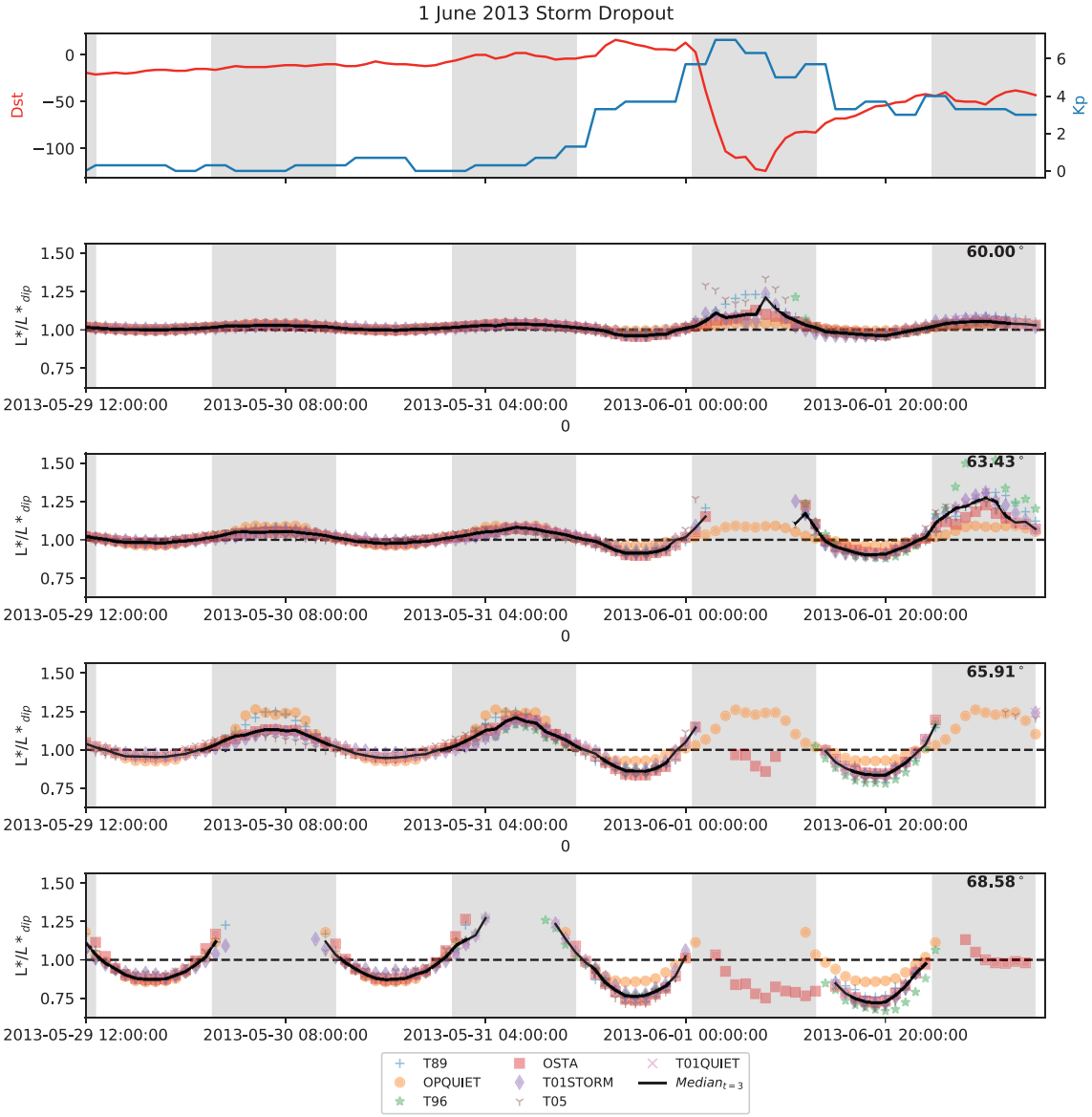

Figure 9. The response of L^* magnetic field models to the June 1, 2013 storm dropout, for the same magnetic latitudes as in Figure 8. This Figure follows the same format as Figure 8.

across these longitudes with caution. We note that for the highest latitude, however, caution should always be taken when making interpolations, and that problems are exacerbated during storm onset. Generally speaking, in any instance where the diurnal variation holds interpolation of L^* across magnetic longitudes should be acceptable.

7. Discussion

In order to use ground observations in radiation belt models, whether for operational applications or for research purposes, usually a single choice must be made of which magnetic field model to use to map the ground location to L^* in the magnetosphere. There are numerous magnetic field models in existence, ranging from analytic to empirical, which generally do not give identical results. Currently, studies make use of a single magnetic field model meaning that subsequent L^* values adhere to ingrained model biases. In operational space weather models of Earth's radiation belts, the use of different magnetic field models

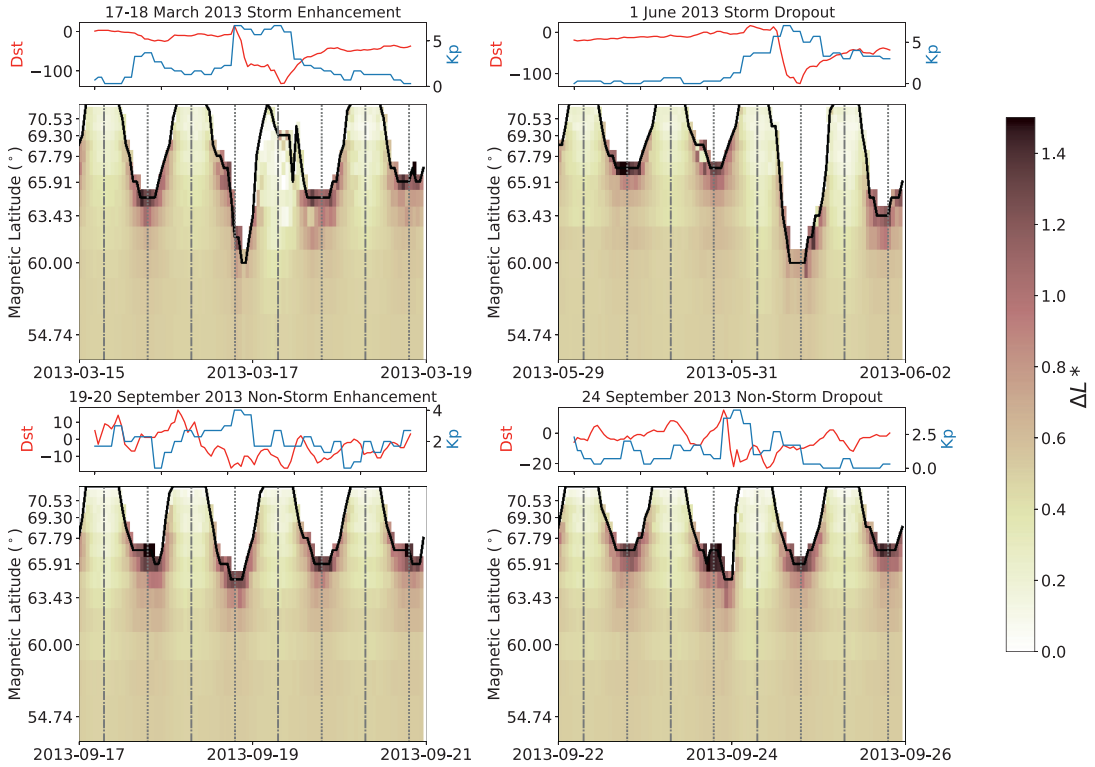

Figure 10. The latitudinal change in L^* (northwards), where L^* is the median of all magnetic field outputs provided that at least three magnetic field models to provide an L^* output (else L^* is assumed to be undefined), shown for the four 2013 GEM challenge events at 330° magnetic longitude. The color in each cell corresponds to the difference in L^* at the particular timestamp between the cell's respective magnetic latitude (y-axis) and the magnetic latitude immediately below in the Pro-L^* domain. The boundary for monotonic increases is illustrated with a black line. Vertical lines for midday (dash-dot) and midnight (dotted) are also shown. The Dst and Kp indices are provided above each event.

for L^* is just one of many sources of uncertainty in the model. However, it is an important source of uncertainty, since L^* is used throughout the construction of radiation belt models, from the wave databases that provide diffusion (e.g., Horne et al., 2018) to the construction of spatial boundary conditions (e.g., Glauert et al., 2018), to the computations within the model itself (e.g., Loridan et al., 2019). Here, we have attempted to quantify the uncertainty, and demonstrate where there may be systematic bias between one magnetic field model and another. In results presented in this manuscript, we found that within regions where ground-to-space mapped L^* is defined for all magnetic field models, the global structure and values for "typical" (median) values were very similar. Notwithstanding any variability, decisions to use a singular model are therefore not too damaging provided modeling is of a climatological nature (modeling how average conditions change over longer time periods). Variability is also small enough (with an IQR ceiling of 0.1 L^*) for ground magnetometers below 60° (66°) on the nightside (dayside) that singular model use may still be warranted. However, while shapes of the L^* distributions for each magnetic field model share some similarities at a number of latitudes (see Figure 5), the variabilities in L^* are notable and arbitrary decisions to use a single model will introduce systematic biases which propagate through all further analysis. These biases are evident in Figures 8 and 9 (and Figures S4 and S5 in Supporting Information) with clear systematic differences in L^* between models in the quiet period prior to event onset, which are naturally amplified on the nightside.

We revisit the proposition by Roederer and Lejosne (2018) that L^* for equatorial pitch angles should be given as default in data packages and computed with a "reliable magnetic field model." Based on the model uncertainty found in our results (an extension of the underlying physical variability in L^*), determination of a reliable magnetic field model is not straightforward. Not only are they configured on a number of (not necessarily the same) complex interacting current systems and driving parameters, they are also approximations to the magnetic field geometry only with no way to benchmark against a true state. The distinction

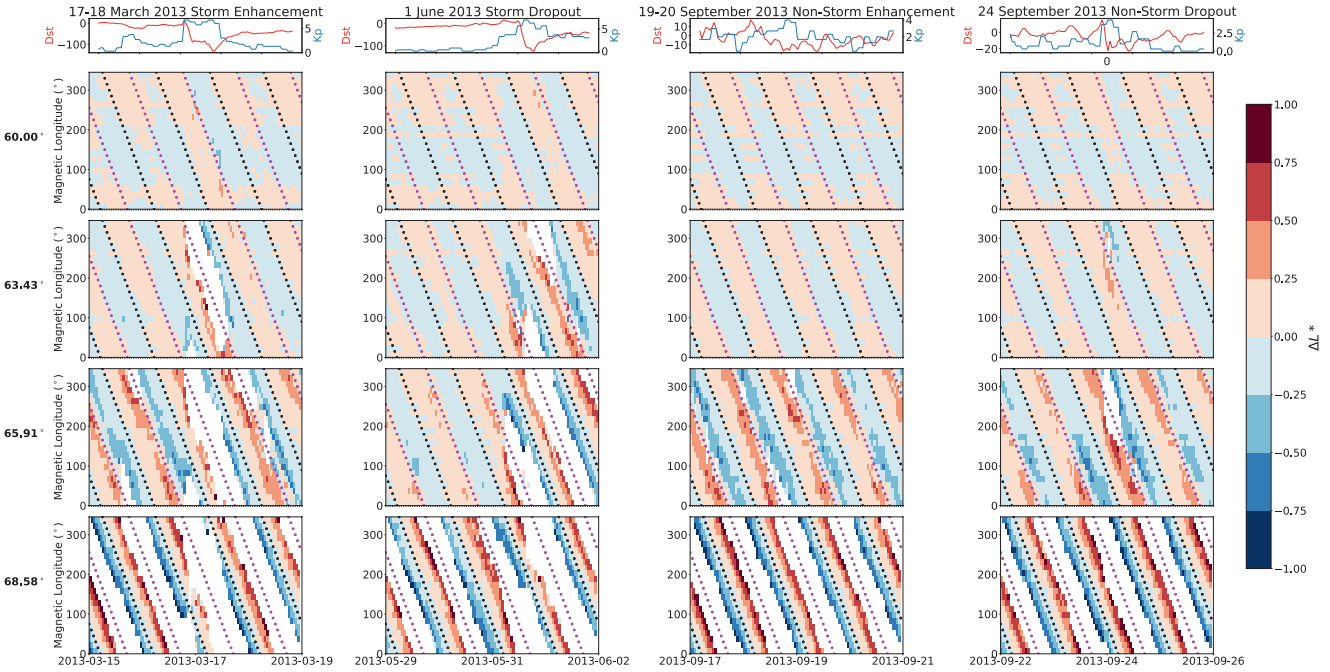

Figure 11. The longitudinal change in L^* (eastwards), where L^* is the median of all magnetic field outputs provided that at least three magnetic field models to provide an L^* output (else L^* is assumed to be undefined), shown for the four 2013 GEM challenge events (columns) and a selection of magnetic latitudes (rows). The color in each cell corresponds to the difference in L^* at the particular timestamp between the cell's respective magnetic longitude (y-axis) and the magnetic longitude immediately west in the Pro-L^* domain. Markers for midday (black-dot) and midnight (pink-dot) are also shown. The Dst and Kp indices are provided over each event in the top row.

between reliability as accuracy instead of reliability as availability is also vital. Since L^* is a property of stably trapped particles and not a physical location, knowledge of its existence is as important as its estimated value. In numerical modeling of processes across a fixed mesh, time-varying latitudinal extents of L^* existence can prove problematic. This could be overcome by opting for the analytic OPQUIET model to reliably guarantee L^* values in the domain, but at the cost of some inaccuracies. Modeling should be informed by accurate L^* values, which should fail gracefully when unavailable, rather than reporting best guesses under all conditions which may result in poor approximations. Reliability of a magnetic field model should therefore accurately decide when L^* is unphysical and provide plausible values for when it is. Unfortunately, quantifying these criteria for comparison across individual magnetic field models is complex.

We have presented a possible solution to these complications in the form of Pro-L^*, an extensive database of L^* approximations (and other magnetospheric parameters) made by several popular magnetic field models, covering a high-resolution domain. Pro-L^* provides the potential to combine L^* values and distributions from magnetic field models probabilistically, reducing and quantifying the uncertainty associated with a single model choice. It also allows us to highlight when the description of L^* as a physical entity is not appropriate. As an illustration, we constructed simple probabilistic L^* models based solely on the number of magnetic field models providing an L^* output (Figures 6 and 7), a proxy for uncertainty in L^* existence. For accepted times of existence the median of returned L^* values is taken in an attempt to further remove model uncertainty. This approach highlighted significant risks when opting for particular magnetic field models, notably OSTA, which exhibited unphysical L^* distributions on the nightside. Physical distributions are observed once we require at least three magnetic field model outputs, with the increase of the model number threshold eroding the boundary of L^* existence to lower latitudes on the nightside. This calls attention to the simplicity of the probabilistic models. The existence of L^* is more advanced than the frequency of returned values. We have mentioned that magnetic field models are configured on a number of current systems with complex interactions, and there appears to be significant disagreements between models at higher latitudes on the nightside. However, the complexity of some models may yield physical results in these regions, and should not be discarded based on simultaneous model outputs alone. A simple median which applies equal

weighting to all magnetic field models is therefore unfeasible in some regions. Developing on the previous argument for L^* existence, L^* values for certain models in regions of high disagreement should be given more weight. We have also observed clustering of models during varying levels of geomagnetic activity (Figures 8 and 9) which can act as an indicator for the best estimate of L^*.

At this stage any choice of weighting is completely arbitrary. Our next step in the development of Pro-L^* is to find a quantitative way to benchmark the considered magnetic field models to deduce effective model weight values and L^* existence, as a function of space and time (with potential separation into quiet and storm time models). One possibility to achieve this is to compare magnetic field model performance against a range of error metrics. This has already been done independently for some of the magnetic field models considered in this study (see Brito & Morley, 2017; Huang et al., 2008; McCollough et al., 2008), but has also been part of model configurations initially. For example, after its configuration Ostapenko and Maltsev (1997) compared their models performance against T89 by the residual sum of squares. To remove systematic model bias entirely we could also benchmark estimated parameters against colocated satellite measurements. Following successful benchmarking we can construct more sophisticated probabilistic models to reduce model uncertainty.

In its current form Pro-L^* may be used directly for both deterministic and probabilistic modeling. For each individual magnetic field model included in Pro-L^* we have tabulated global L^* statistics (in magnetic latitude and MLT) which can be rapidly imported and attached to ground observations for implementation in radiation belt studies. The statistics include both the arithmetic median and mean as averages, with value uncertainty quantified by the IQR and existence uncertainty quantified by normalized occurrence statistics (see Supporting Information). In addition to these, we have also tabulated the same statistics for the simple global probabilistic L^* models presented in Section 4.2. All data sets have been provided alongside this manuscript.

We have not investigated uncertainties which can be introduced into the calculation of L^* using other numerical tracing methods. Other methods exist, including LANLGeoMag (Henderson et al., 2018), AFRL-Shell (see Albert et al., 2018), and LANLstar (Yu et al. [2012], also within SpacePy [Morley et al., 2010]) which each have different benefits and problems. Some methods are better for drift orbit bifurcations, for example (see Albert et al. (2018), for a discussion). Our presentation of Pro-L^* in this work demonstrates how further uncertainties, such as those resulting from different numerical methods, could be incorporated into the probabilistic model.

In its current incarnation, model uncertainties culminated over the 11-year period in Pro-L^* are significant, with physical uncertainties contained within. It may be that parameterization of Pro-L^* probabilistic models could further reduce these uncertainties and produce better utility of the models. However, the choice of parameters to use requires thought, given the different inputs required for different magnetic field models and the fact that not all magnetic field models are independent.

For the ground-based Pro-L^*, it may be important to determine sources of uncertainty in mapping the ground-location to the magnetic field minimum, and sources of uncertainty in tracing out the field globally in order to estimate L^*. Future improvements to Pro-L^* will involve finding the sources of uncertainty. Assessing ionospheric-magnetospheric mapping is complex, however, as there is no conventional method for model validation. Attempts have been made to deduce mapping accuracy from the angular error in the direction of the magnetic field vector relative to magnetic field observations (Brito & Morley, 2017; Pulkkinen & Tsyganenko, 1996), but this does not guarantee the accurate location of the ionospheric footprint. More complex approaches compare magnetically conjugate phenomena at the ionosphere and along the field line in the magnetosphere. For example, Weiss et al. (1997) compared electron spectra measurements between Defense Meteorological Satellite Program at low altitudes with geosynchronous Los Alamos National Laboratory (LANL) spacecraft, while Shevchenko et al. (2010) explored the isotropy boundary of precipitation of energetic particles deduced by low-altitude spacecraft, wherein particles are observed at ionospheric latitudes but their precipitation is governed by the magnetic field near the equator.

Pro-L^* is freely available in its current incarnation both as a data set (available at http://dx.doi.org/10.17864/1947.222) where we supply L^* values (and related variables) calculated using the seven outlined magnetic field models over our specified high resolution spatial grid throughout 2006–2016, and a

freely available Python package (available at https://github.com/Rhyst223/pro-lstar.git). In the initial Python package release, users are able to quickly generate data for specific dates and ground locations relative to the Pro-L^* data set (with built-in interpolation for off-grid locations), and automatically generate plots similar to the ones shown in this manuscript for the 2013 GEM challenge events. Global L^* statistics (mean, median, IQR, and occurrence rate) for all gridpoints in the Pro-L^* (decomposed into magnetic latitude × MLT) are also provided in the Supporting Information as readable data sets, including statistics for each individual external magnetic field model and the simple probabilistic models in Section 4.2. Statistics for the former are also given as tables in the Supporting Information. All subsequent improvements will be incorporated into the Python package and some the future planned developments are as follows:

- Statistical quantities for both user specified and predefined model weightings.
- Generation of user-specified latitude and MLT based probabilistic L^* distributions, parameterized by appropriate physical quantities or tuned to predetermined model accuracies, with interpolation managed under the hood when the specified location does not fall precisely on our grid in Figure 1.
- L^* forecasting capabilities.

8. Conclusion

In this paper, we have presented for the first time a probabilistic aid for mapping ground observations to L^*, Pro-L^*, which combines results from several magnetic field models in an extensive data set. Pro-L^* covers a high resolution grid of ground locations in magnetic latitude, longitude, and MLT in the Northern Hemisphere, where the majority of ground instruments are located. Although the climatological structure of L^* is consistent between most magnetic field models, significant L^* variability exists across large regions of magnetic latitude and MLT on typical timescales of interest due to both systematic model biases and physical variability from magnetospheric processes. We have illustrated approaches to determine L^* probabilistically which removes some of the observed systematic biases, and also quantified this uncertainty. These illustrations were considered both in a distribution sense and real-life test cases. The possibility of L^* interpolation across gridpoints in probabilistic models was explored, and criteria for successful interpolation determined. The extension of Pro-L^* from its current form as a data set into a fully functional Python package has been outlined, with the initial release locatable at https://github.com/Rhyst223/pro-lstar.git. The full Pro-L^* data set is available at http://dx.doi.org/10.17864/1947.222.

Acknowledgments
RLT is supported by the Engineering and Physical Sciences Research Council (EPSRC) (Grant no. EP/L016613/1). Contributions to this work by SKM were performed under the auspices of the U.S. Department of Energy and were supported by the U.S. Department of Energy Laboratory Directed Research and Development program award 20190262ER. This research used resources provided by the Los Alamos National Laboratory Institutional Computing Program, which is supported by the U.S. Department of Energy National Nuclear Security Administration under Contract No. 89233218CNA000001. This research has been approved for unlimited release and has been assigned the number LA-UR-20-25,802. CEJW is supported by Natural Environment Research Council (NERC) (Grant no. NE/P017274/1) and Science and Technology Facilities Council (STFC) (Grant no. ST/R000921/1). SNB is supported by Science and Technology Facilities Council (STFC) (Grant no. ST/R000921/1). PDW is supported by the Royal Society (Grant no. UF130571).

Data Availability Statement

Pro-L^* data set is freely available at http://dx.doi.org/10.17864/1947.222. The most up-to-date release of the Pro-L^* Python package is available at https://github.com/Rhyst223/pro-lstar.git. Information on the GEM challenge events is available at http://bit.ly/28UnLpw.

References

Albert, J. M., Selesnick, R. S., Morley, S. K., Henderson, M. G., & Kellerman, A. C. (2018). Calculation of last closed drift shells for the 2013 GEM radiation belt challenge events. *Journal of Geophysical Research: Space Physics*, *123*(11), 9597–9611. https://doi.org/10.1029/2018JA025991

Angelopoulos, V. (2008). The THEMIS mission. *Space Science Reviews*, *141*(1–4), 5–34. https://doi.org/10.1007/s11214-008-9336-1

Boscher, B. S. O. T. P. (2013). *The International Radiation Belt Environment Modeling (IRBEM) library*. Retrieved from https://sourceforge.net/projects/irbem/

Boyd, A. J., Spence, H. E., Claudepierre, S. G., Fennell, J. F., Blake, J. B., Baker, D. N., et al. (2014). Quantifying the radiation belt seed population in the 17 March 2013 electron acceleration event. *Geophysical Research Letters*, *41*(7), 2275–2281. https://doi.org/10.1002/2014GL059626

Brito, T. V., & Morley, S. K. (2017). Improving empirical magnetic field models by fitting to in situ data using an optimized parameter approach. *Space Weather*, *15*(12), 1628–1648. https://doi.org/10.1002/2017SW001702

Burrell, A. G., Halford, A., Klenzing, J., Stoneback, R. A., Morley, S. K., Annex, A. M., et al. (2018). Snakes on a spaceship—An overview of Python in heliophysics. *Journal of Geophysical Research: Space Physics*, *123*(12), 10384–10402. https://doi.org/10.1029/2018JA025877

Capannolo, L., Li, W., Ma, Q., Zhang, X., Redmon, R. J., Rodriguez, J. V., et al. (2018). Understanding the driver of energetic electron precipitation using coordinated multisatellite measurements. *Geophysical Research Letters*, *45*(14), 6755–6765. https://doi.org/10.1029/2018GL078604

Carter, J. A., Milan, S. E., Coxon, J. C., Walach, M., & Anderson, B. J. (2016). Average field-aligned current configuration parameterized by solar wind conditions. *Journal of Geophysical Research: Space Physics*, *121*(2), 1294–1307. https://doi.org/10.1002/2015JA021567

Clilverd, M. A., Duthie, R., Hardman, R., Hendry, A. T., Rodger, C. J., Raita, T., et al. (2015). Electron precipitation from EMIC waves: A case study from 31 May 2013. *Journal of Geophysical Research: Space Physics*, *120*(5), 3618–3631. https://doi.org/10.1002/2015JA021090

Fairfield, D. H., & Mead, G. D. (1975). Magnetospheric mapping with a quantitative geomagnetic field model. *Journal of Geophysical Research*, *80*(4), 535–542. https://doi.org/10.1029/JA080i004p00535

Fairfield, D. H., Tsyganenko, N. A., Usmanov, A. V., & Malkov, M. V. (1994). A large magnetosphere magnetic field database. *Journal of Geophysical Research*, *99*(A6), 11319. https://doi.org/10.1029/94JA00255

Fei, Y., Chan, A. A., Elkington, S. R., & Wiltberger, M. J. (2006). Radial diffusion and MHD particle simulations of relativistic electron transport by ULF waves in the September 1998 storm. *Journal of Geophysical Research: Space Physics*, *111*(A12). https://doi.org/10.1029/2005JA011211

Finlay, C. C., Maus, S., Beggan, C. D., Bondar, T. N., Chambodut, A., Chernova, T. A., et al. (2010). International Geomagnetic Reference Field: The eleventh generation. *Geophysical Journal International*, *183*(3), 1216–1230. https://doi.org/10.1111/j.1365-246X.2010.04804.x

Forsyth, C., Rae, I. J., Coxon, J. C., Freeman, M. P., Jackman, C. M., Gjerloev, J., & Fazakerley, A. N. (2015). A new technique for determining Substorm Onsets and Phases from Indices of the Electrojet (SOPHIE). *Journal of Geophysical Research: Space Physics*, *120*(12), 592–610. https://doi.org/10.1002/2015JA021343

Ganushkina, N. Y., Liemohn, M. W., Kubyshkina, M. V., Ilie, R., & Singer, H. J. (2010). Distortions of the magnetic field by storm-time current systems in Earth's magnetosphere. *Annales Geophysicae*, *28*(1), 123–140. https://doi.org/10.5194/angeo-28-123-2010

Glauert, S. A., Horne, R. B., & Meredith, N. P. (2018). A 30-year simulation of the outer electron radiation belt. *Space Weather*, *16*(10), 1498–1522. https://doi.org/10.1029/2018SW001981

Haiducek, J. D., Welling, D. T., Morley, S. K., Ganushkina, N. Y., & Chu, X. (2020). Using multiple signatures to improve accuracy of substorm identification. *Journal of Geophysical Research: Space Physics*, *125*(4). https://doi.org/10.1029/2019JA027559

Henderson, M., Morley, S., Niehof, J., & Larsen, B. (2018). *drsteve/LANLGeoMag: v1.5.16*. Retrieved from https://zenodo.org/record/1195041#.XTiCoJNKgWo; https://doi.org/10.5281/ZENODO.1195041

Horne, R. B., Phillips, M. W., Glauert, S. A., Meredith, N. P., Hands, A. D. P., Ryden, K. A., & Li, W. (2018). Realistic worst case for a severe space weather event driven by a fast solar wind stream. *Space Weather*, *16*(9), 1202–1215. https://doi.org/10.1029/2018SW001948

Huang, C.-L. L., Spence, H. E., Singer, H. J., Tsyganenko, N. A., Huang, C.-L., Spence, H. E., et al. (2008). A quantitative assessment of empirical magnetic field models at geosynchronous orbit during magnetic storms Recommended Citation A quantitative assessment of empirical magnetic field models at geosynchronous orbit during magnetic storms. *Journal of Geophysical Research*, *113*, 4208. https://doi.org/10.1029/2007JA012623

Hudson, M. K., Paral, J., Kress, B. T., Wiltberger, M., Baker, D. N., Foster, J. C., et al. (2015). Modeling CME-shock-driven storms in 2012-2013: MHD test particle simulations. *Journal of Geophysical Research: Space Physics*, *120*(2), 1168–1181. https://doi.org/10.1002/2014JA020833

Kang, S.-B., Fok, M.-C., Komar, C., Glocer, A., Li, W., & Buzulukova, N. (2018, 2). An energetic electron flux dropout due to magnetopause shadowing on 1 June 2013. *Journal of Geophysical Research: Space Physics*, *123*(2), 1178–1190. https://doi.org/10.1002/2017JA024879

Kubyshkina, M., Sergeev, V., Tsyganenko, N., Angelopoulos, V., Runov, A., Donovan, E., et al. (2011). Time-dependent magnetospheric configuration and breakup mapping during a substorm. *Journal of Geophysical Research: Space Physics*, *116*, A00I27. https://doi.org/10.1029/2010JA015882

Li, Z., Hudson, M., Kress, B., & Paral, J. (2015). Three-dimensional test particle simulation of the 17-18 March 2013 CME shock-driven storm. *Geophysical Research Letters*, *42*(14), 5679–5685. https://doi.org/10.1002/2015GL064627

Li, W., Thorne, R. M., Ma, Q., Ni, B., Bortnik, J., Baker, D. N., et al. (2014). Radiation belt electron acceleration by chorus waves during the 17 March 2013 storm. *Journal of Geophysical Research: Space Physics*, *119*(6), 4681–4693. https://doi.org/10.1002/2014JA019945

Loridan, V., Ripoll, J., Tu, W., & Scott Cunningham, G. (2019). On the use of different magnetic field models for simulating the dynamics of the outer radiation belt electrons during the october 1990 storm. *Journal of Geophysical Research: Space Physics*, *124*(8), 6453–6486. https://doi.org/10.1029/2018JA026392

Ma, Q., Li, W., Bortnik, J., Thorne, R. M., Chu, X., Ozeke, L. G., et al. (2018). Quantitative evaluation of radial diffusion and local acceleration processes during GEM challenge events. *Journal of Geophysical Research: Space Physics*, *123*(3), 1938–1952. https://doi.org/10.1002/2017JA025114

Mann, I. R., Milling, D. K., Rae, I. J., Ozeke, L. G., Kale, A., Kale, Z. C., et al. (2008). The upgraded CARISMA magnetometer array in the THEMIS era. *Space Science Reviews*, *141*(1–4), 413–451. https://doi.org/10.1007/s11214-008-9457-6

McCollough, J. P., Gannon, J. L., Baker, D. N., & Gehmeyr, M. (2008). A statistical comparison of commonly used external magnetic field models. *Space Weather*, *6*, S10001. https://doi.org/10.1029/2008SW000391

McIlwain, C. E. (1961). Coordinates for mapping the distribution of magnetically trapped particles. *Journal of Geophysical Research*, *66*(11), 3681–3691. https://doi.org/10.1029/JZ066i011p03681

Morley, S. K., Welling, D. T., Koller, J., Larsen, B. A., Henderson, M. G., & Niehof, J. (2010). *SpacePy-A Python-based Library of Tools for the Space Sciences (Tech. Rep.)*. Retrieved from http://spacepy.lanl.gov

Morley, S. K., Welling, D. T., & Woodroffe, J. R. (2018). Perturbed input ensemble modeling with the space weather modeling framework. *Space Weather*, *16*(9), 1330–1347. https://doi.org/10.1029/2018SW002000

Olifer, L., Mann, I. R., Morley, S. K., Ozeke, L. G., & Choi, D. (2018). On the role of last closed drift shell dynamics in driving fast losses and Van Allen radiation belt extinction. *Journal of Geophysical Research: Space Physics*, *123*(5), 3692–3703. https://doi.org/10.1029/2018JA025190

Olson, W. P., & Pfitzer, K. A. (1974). A quantitative model of the magnetospheric magnetic field. *Journal of Geophysical Research*, *79*(25), 3739–3748. https://doi.org/10.1029/JA079i025p03739

Orr, L., Chapman, S. C., & Gjerloev, J. W. (2019). Directed network of substorms using SuperMAG ground-based magnetometer data. *Geophysical Research Letters*, *46*(12), 6268–6278. https://doi.org/10.1029/2019GL082824

Ostapenko, A. A., & Maltsev, Y. P. (1997). Relation of the magnetic field in the magnetosphere to the geomagnetic and solar wind activity. *Journal of Geophysical Research: Space Physics*, *102*(A8), 17467–17473. https://doi.org/10.1029/97JA00937

Ozeke, L. G., Mann, I. R., Murphy, K. R., Jonathan Rae, I., & Milling, D. K. (2014). Analytic expressions for ULF wave radiation belt radial diffusion coefficients. *Journal of Geophysical Research: Space Physics*, *119*(3), 1587–1605. https://doi.org/10.1002/2013JA019204

Ozeke, L. G., Mann, I. R., Murphy, K. R., Rae, I. J., Milling, D. K., Elkington, S. R., et al. (2012). ULF wave derived radiation belt radial diffusion coefficients. *Journal of Geophysical Research*, *117*(A4). https://doi.org/10.1029/2011JA017463

Pakhotin, I. P., Drozdov, A. Y., Shprits, Y. Y., Boynton, R. J., Subbotin, D. A., & Balikhin, M. A. (2014). Simulation of high-energy radiation belt electron fluxes using NARMAX-VERB coupled codes. *Journal of Geophysical Research: Space Physics*, *119*(10), 8073–8086. https://doi.org/10.1002/2014JA020238

Pulkkinen, T. I., & Tsyganenko, N. A. (1996). Testing the accuracy of magnetospheric model field line mapping. *Journal of Geophysical Research: Space Physics*, *101*(A12), 27431–27442. https://doi.org/10.1029/96ja02489

Qin, Z., Denton, R. E., Tsyganenko, N. A., & Wolf, S. (2007). Solar wind parameters for magnetospheric magnetic field modeling. *Space Weather*, *5*(11), S11003. https://doi.org/10.1029/2006SW000296

Roederer, J. G. (1970). *Dynamics of geomagnetically trapped radiation*. Berlin: Springer-Verlag.

Roederer, J. G., & Lejosne, S. (2018). Coordinates for representing radiation belt particle flux. *Journal of Geophysical Research: Space Physics*, *123*(2), 1381–1387. https://doi.org/10.1002/2017JA025053

Roederer, J. G., & Zhang, H. (2014). *Dynamics of magnetically trapped particles* (Vol. 403). Berlin, Heidelberg: Springer Berlin Heidelberg. https://doi.org/10.1007/978-3-642-41530-2

Scott, D. W. (1979). On optimal and data-based histograms. *Biometrika*, *66*(3), 605–610.Retrieved from https://academic.oup.com/biomet/article-abstract/66/3/605/232642

Shevchenko, I. G., Sergeev, V., Kubyshkina, M., Angelopoulos, V., Glassmeier, K. H., & Singer, H. J. (2010). Estimation of magnetosphere-ionosphere mapping accuracy using isotropy boundary and THEMIS observations. *Journal of Geophysical Research: Space Physics*, *115*, A11206. https://doi.org/10.1029/2010JA015354

Shprits, Y. Y., Kellerman, A. C., Drozdov, A. Y., Spence, H. E., Reeves, G. D., & Baker, D. N. (2015). Combined convective and diffusive simulations: VERB-4D comparison with 17 March 2013 Van Allen probes observations. *Geophysical Research Letters*, *42*(22), 9600–9608. https://doi.org/10.1002/2015GL065230

Sibeck, D. G., & Angelopoulos, V. (2008). THEMIS science objectives and mission phases. *Space Science Reviews*, *141*(1–4), 35–59. https://doi.org/10.1007/s11214-008-9393-5

Su, Z., Gao, Z., Zhu, H., Li, W., Zheng, H., Wang, Y., et al. (2016). Nonstorm time dropout of radiation belt electron fluxes on 24 September 2013. *Journal of Geophysical Research: Space Physics*, *121*(7), 6400–6416. https://doi.org/10.1002/2016JA022546

Thébault, E., Finlay, C. C., Beggan, C. D., Alken, P., Aubert, J., Barrois, O., et al. (2015). International Geomagnetic Reference Field: The 12th generation. *Earth, Planets and Space*, *67*(1), 79. https://doi.org/10.1186/s40623-015-0228-9

Tsyganenko, N. A. (1989). A magnetospheric magnetic field model with a warped tail current sheet. *Planetary and Space Science*, *37*(1), 5–20. https://doi.org/10.1016/0032-0633(89)90066-4

Tsyganenko, N. A. (1995). Modeling the Earth's magnetospheric magnetic field confined within a realistic magnetopause. *Journal of Geophysical Research*, *100*(A4), 5599. https://doi.org/10.1029/94JA03193

Tsyganenko, N. A. (1996). Effects of the solar wind conditions on the global magnetospheric configuration as deduced from data-based field models. Retrieved from https://ntrs.nasa.gov/search.jsp?R=19970016534

Tsyganenko, N. A. (2002a). A model of the near magnetosphere with a dawn-dusk asymmetry 1. Mathematical structure. *Journal of Geophysical Research*, *107*(A8), 12–21. https://doi.org/10.1029/2001JA000219

Tsyganenko, N. A. (2002b). A model of the near magnetosphere with a dawn-dusk asymmetry 2. Parameterization and fitting to observations. *Journal of Geophysical Research*, *107*(A8), 10–11. https://doi.org/10.1029/2001JA000220

Tsyganenko, N. A. (2013). Data-based modeling of the Earth's dynamic magnetosphere: A review. *Annales Geophysicae*, *31*(10), 1745–1772. https://doi.org/10.5194/angeo-31-1745-2013

Tsyganenko, N. A., & Andreeva, V. A. (2016). An empirical RBF model of the magnetosphere parameterized by interplanetary and ground-based drivers. *Journal of Geophysical Research: Space Physics*, *121*(11), 786–810. https://doi.org/10.1002/2016JA023217

Tsyganenko, N. A., & Andreeva, V. A. (2017). A hybrid approach to empirical magnetosphere modeling. *Journal of Geophysical Research: Space Physics*, *122*(8), 8198–8213. https://doi.org/10.1002/2017JA024359

Tsyganenko, N. A., Singer, H. J., & Kasper, J. C. (2003). Storm-time distortion of the inner magnetosphere: How severe can it get?. *Journal of Geophysical Research: Space Physics*, *108*, A51209. https://doi.org/10.1029/2002JA009808

Tsyganenko, N. A., & Sitnov, M. I. (2005). Modeling the dynamics of the inner magnetosphere during strong geomagnetic storms. *Journal of Geophysical Research*, *110*(A3), A03208. https://doi.org/10.1029/2004JA010798

Tu, W., Li, W., Albert, J. M., & Morley, S. K. (2019, 2). Quantitative assessment of radiation belt modeling. *Journal of Geophysical Research: Space Physics*, *124*(2), 898–904. https://doi.org/10.1029/2018JA026414

Ukhorskiy, A. Y., Sitnov, M. I., Millan, R. M., Kress, B. T., Fennell, J. F., Claudepierre, S. G., & Barnes, R. J. (2015). Global storm time depletion of the outer electron belt. *Journal of Geophysical Research: Space Physics*, *120*(4), 2543–2556. https://doi.org/10.1002/2014JA020645

Wang, C., Ma, Q., Tao, X., Zhang, Y., Teng, S., Albert, J. M., et al. (2017). Modeling radiation belt dynamics using a 3-D layer method code. *Journal of Geophysical Research: Space Physics*, *122*(8), 8642–8658. https://doi.org/10.1002/2017JA024143

Wang, C. P., Xing, X., Liu, Y. H., & Runov, A. (2018). A case study of connection between ground magnetic field perturbations and tail current sheet bursty flows at X=60RE. *Journal of Geophysical Research: Space Physics*, *123*(3), 1822–1833. https://doi.org/10.1002/2017JA024972

Watt, C. E. J., Allison, H. J., Meredith, N. P., Thompson, R. L., Bentley, S. N., Rae, I. J., et al. (2019). Variability of quasilinear diffusion coefficients for plasmaspheric hiss. *Journal of Geophysical Research: Space Physics*, *124*(11), 8488–8506. https://doi.org/10.1029/2018JA026401

Weiss, L. A., Thomsen, M. F., Reeves, G. D., & McComas, D. J. (1997). An examination of the Tsyganenko (T89a) field model using a database of two-satellite magnetic conjunctions. *Journal of Geophysical Research: Space Physics*, *102*(A3), 4911–4918. https://doi.org/10.1029/96JA02876

Xiao, F., Yang, C., He, Z., Su, Z., Zhou, Q., He, Y., et al. (2014). Chorus acceleration of radiation belt relativistic electrons during March 2013 geomagnetic storm. *Journal of Geophysical Research: Space Physics*, *119*(5), 3325–3332. https://doi.org/10.1002/2014JA019822

Xu, Z., Hartinger, M. D., Clauer, C. R., Peek, T., & Behlke, R. (2017). A comparison of the ground magnetic responses during the 2013 and 2015 St. Patrick's Day geomagnetic storms. *Journal of Geophysical Research: Space Physics*, *122*(4), 4023–4036. https://doi.org/10.1002/2016JA023338

Yu, Y., Koller, J., Zaharia, S., & Jordanova, V. (2012). L* neural networks from different magnetic field models and their applicability. *Space Weather*, *10*(2). https://doi.org/10.1029/2011SW000743